

Thermal Comfort Analysis Inside of a Recreational Vehicle

by

Mahboubeh Taftian

A thesis
presented to the University of Waterloo
in fulfillment of the
thesis requirement for the degree of
Master of Applied Science
in
Mechanical and Mechatronics Engineering

Waterloo, Ontario, Canada, 2020

© Mahboubeh Taftian 2020

Author's Declaration

I hereby declare that I am the sole author of this thesis. This is a true copy of the thesis, including any required final revisions, as accepted by my examiners.

I understand that my thesis may be made electronically available to the public.

Abstract

The focus of the current study is on the numerical investigation of airflow and temperature distribution in a representative Class B Recreational Vehicle (RV) with the objective of optimizing the inlet and exhaust vent configurations to enhance thermal comfort levels. The Computational Fluid Dynamics (CFD) simulations are carried out using ANSYS FLUENT. The CFD model of a representative RV is described in detail. First, a reference case that is based on the existing RV model is presented. For further optimizations with respect to this reference case, a parametric study is performed. This parametric study focuses on evaluating the impact of inlet and outlet vent locations, supply airflow direction, and varying the number of exhaust vents on temperature and airflow distributions. Seven test cases are simulated in total. The simulation results are evaluated based on their temperatures, velocity magnitudes, PMV (Predicted Mean Vote), and PPD (Predicted Percentage of Dissatisfied) values.

Dedication

This thesis is dedicated to

the memory of my mom who raised me to be the person I am today, and my family and friends without whom it was almost impossible for me to complete my thesis work.

Table of Contents

List of Tables	viii
List of Figures	ix
1 Introduction	1
1.1 Research Importance	1
1.2 Literature Review	2
1.2.1 Motivation	11
1.2.2 Objectives	12
1.2.3 Thesis Structure	13
2 Numerical Method and Validation Case	14
2.1 Numerical Modeling	14
2.1.1 Governing Equations	15
2.1.2 Turbulence modeling	16
2.1.3 Boundary Conditions	19

2.1.4	Mesh Generation	20
2.1.5	Boundary Layer	20
2.2	Validation Case	22
2.2.1	Experiment Set-up	24
2.2.2	CFD Simulation Set-up	24
2.2.3	Solver Settings	27
3	Numerical Simulation of Recreational Vehicle Cabin	30
3.1	Numerical model	30
3.1.1	Problem Description	30
3.1.2	Heat Flux Estimations and Boundary Conditions	33
3.1.3	Mesh Generation	36
3.1.4	Selection of Turbulence Model and solver Setting	40
3.1.5	Thermal Comfort Criteria	40
3.1.6	Model Development	43
3.2	Results and Discussion	45
3.2.1	Reference Case	46
3.2.2	RV compartment with and without AC system	51
3.2.3	Impact of the Direction of Supply Air Flow	54
3.2.4	Impact of the location of AC Inlet	59
3.2.5	The Impact of Outlet Location	63

3.2.6	Impact of Number of Exhaust Vents	67
3.2.7	Summary of Results	71
4	Conclusions	74
4.1	Future Work	77
References		78
Appendices		90

List of Tables

2.1	Disadvantages and advantages of different turbulent models [1].	18
2.2	Exterior Walls' Temperatures [2].	26
3.1	Appliances Heat Fluxes [3]	34
3.2	Boundary condition settings for surfaces	36
3.3	Summary of the different mesh size combinations.	38
3.4	ASHRAE thermal sensation scale [4]	41
3.5	Coordinates of allocated measuring lines.	44
3.6	Boundary conditions used in the reference case.	47
3.7	Vent coordinates for cases 3, 4 and the reference case.	60
3.8	Vent coordinates for case 5 and the reference case.	64
3.9	Vent coordinates for case 6 and the reference case.	68

List of Figures

2.1	Element Shapes in 3D meshes, a) tetrahedral b) hexahedron c) prism d) pyramid [5]	21
2.2	Geometry of Room.	25
2.3	Grid discretization of the test room geometry.	25
2.4	Comparison between temperatures at pole.	28
2.5	Comparison between temperatures at line 1.	28
2.6	Distribution of temperature at steady state condition.	29
3.1	Erwin Hymer Aktiv RV Class B.	32
3.2	3D Geometry of the RV's Inner Space (locations of appliances, inlet, and outlet: 1, microwave; 2, television; 3, refrigerator; 4, lamps; 5, cabinets; 6, inverter fan grille; 7, water pump; 8, oven; 9, AC grille; 10, exhaust grille; 11, windshield; 12, windows; 13, furniture; 14, seats)	33
3.3	Focused view of important features.	37
3.4	Mesh independency test (temperature change on the center-line of the cabin, from (0, 1.0135, 0) to (5.045, 1.0135, 0)) at time t=60s.	38

3.5	Mesh independency test (velocity change on the center-line of the cabin, from (0, 1.0135, 0) to (5.045, 1.0135, 0)) at time t=60s.	39
3.6	Selected computational mesh.	39
3.7	Contours of reference case at $t = 200s$: (a) temperature distribution and (b) velocity magnitude at $Z = 0$ (XY Plane).	48
3.8	Contours of reference case at $t = 200s$: (a) temperature distribution and (b) velocity magnitude at $X = 0.86m$, $X = 2.4m$, and $X = 4.5m$ (YZ Planes) .	49
3.9	Temperature profiles at $t = 200s$ along (a)line 1, (b)line 2, and (c)line 3. .	50
3.10	PMV profiles at $t = 200s$ along vertical lines at (a)line 1, (b)line 2, and (c)line 3.	50
3.11	PPD profiles at $t = 200s$ along vertical lines at (a)line 1, (b)line 2, and (c)line 3.	50
3.12	Transient simulation of spatially-averaged temperature for reference case. .	51
3.13	Temperature distribution at $Z = 0 m$ for reference case.	51
3.14	Temperature profiles at $t = 200s$ along (a) line 1, (b) line 2, and (c) line 3.	52
3.15	Temperature distribution at $Z = 0m$ (a) reference case (b) case without AC ($t = 200s$).	53
3.16	Velocity magnitude at $Z = 0m$ (a) reference case (b) case without AC ($t = 200s$).	53
3.17	Temperature distribution at $X = 0.86m$, $X = 2.4m$, and $X = 4.5m$ (a) reference case (b) case without AC ($t = 200s$).	54
3.18	Schematic of velocity vectors.	55

3.19	Temperature distribution at $Z = 0m$ for (a) case 1 (b) case 2 ($t = 200s$)	56
3.20	Velocity magnitude at $Z = 0m$ for (a) case 1 (b) case 2 ($t = 200s$)	56
3.21	Temperature distribution at $X = 0.86m, X = 2.4m, X = 4.5m$ for (a) case 1 (b) case 2 ($t = 200s$)	57
3.22	Velocity magnitude at $X = 0.86m, X = 2.4m, X = 4.5m$ for (a) case 1 (b) case 2 ($t = 200s$)	57
3.23	Temperature profiles for case 1, case 2, and reference case along (a) line 1, (b) line 2, and (c) line 3 ($t = 200s$)	58
3.24	PMV profiles for case 1, case 2, and reference case along (a) line 1, (b) line 2, and (c) line 3 ($t = 200s$)	58
3.25	PPD profiles for case 1, case 2, and reference case along (a) line 1, (b) line 2, and (c) line 3 ($t = 200s$)	59
3.26	Vent locations.	59
3.27	Temperature distribution at $Z = 0m$ for (a) case 3 and (b) case 4 ($t = 200s$) .	61
3.28	Velocity magnitude at $Z = 0m$ for (a) case 3 (b) case 4 ($t = 200s$)	61
3.29	Temperature distribution at $X = 0.86m, X = 2.4m, X = 4.5m$ for (a) case 3 (b) case 4 ($t = 200s$)	61
3.30	Velocity magnitude at $X = 0.86m, X = 2.4m, X = 4.5m$ for (a) case 3 (b) case 4 ($t = 200s$)	62
3.31	Temperature profiles for case 3, case 4, and reference case along (a) line 1, (b) line 2, and (c) line 3 ($t = 200s$)	62
3.32	PMV profiles for case 3, case 4, and reference case along (a) line 1, (b) line 2, and (c) line 3 ($t = 200s$)	63

3.33 PPD profiles for case 3, case 4, and reference case along (a) line 1, (b) line 2, and (c) line 3 ($t = 200s$)	63
3.34 Temperature distribution at $Z = 0m$ for (a) reference case (b) case 5 ($t = 200s$).	64
3.35 Velocity magnitude at $Z = 0m$ for (a) reference case (b) case 5 ($t = 200s$).	65
3.36 Temperature distribution at $X = 0.86m$, $X = 2.4m$, $X = 4.5m$ for (a) reference case (b) case 5 ($t = 200s$).	65
3.37 Velocity magnitude at $x=0.86m$, $x=2.4m$, $x=4.5m$ for (a) reference case (b) case 5 ($t = 200s$).	66
3.38 Temperature profiles for case 5 and reference case along (a) line 1, (b) line 2, and (c) line 3 ($t = 200s$).	66
3.39 PMV profiles for case 5 and reference case along (a) line 1, (b) line 2, and (c) line 3 ($t = 200s$).	67
3.40 PPD profiles for case 5 and reference case along (a) line 1, (b) line 2, and (c) line 3 ($t = 200s$).	67
3.41 Temperature distribution at $Z = 0m$ for (a) reference case (b) case 6 ($t = 200s$).	68
3.42 Velocity magnitude at $Z = 0m$ for (a) reference case (b) case 6 ($t = 200s$).	69
3.43 Temperature distribution at $X = 0.86m$, $X = 2.4m$, $X = 4.5m$ for (a) reference case (b) case 6 ($t = 200s$).	69
3.44 Velocity magnitude at $X = 0.86m$, $X = 2.4m$, $X = 4.5m$ for (a) reference case (b) case 6 ($t = 200s$).	70

3.45 Temperature profiles for case 6, and reference case along (a) line 1, (b) line 2, and (c) line 3 ($t = 200s$)	70
3.46 PMV profiles for case 6 and reference case along (a) line 1, (b) line 2, and (c) line 3 ($t = 200s$)	71
3.47 PPD profiles for case 6 and reference case along (a) line 1, (b) line 2, and (c) line 3 ($t = 200s$)	71
3.48 Transient simulation of spatial-averaged temperature for reference case and case 6 (two outlets at both sides of the inlet vent)	73

Chapter 1

Introduction

1.1 Research Importance

One of the most important and critical concerns about human efficiency in daily life is thermal comfort. In the current modernized world, the increasing dependence on new technologies leads people to spend a significant portion of their time in enclosed environments, which is thermally controlled by cooling and heating systems. Yet, it has been discovered that HVAC systems (Heating, Ventilation, and Air Conditioning) energy usage contributes to 20% of the total national energy consumption in Europe and the USA and 50% of the total energy consumption in buildings [6]. Moreover, in tropical climates, the energy consumption of a typical HVAC system in a building exceeds 50% [7].

Since the sense of comfort in the same environment differs from one person to the other, several definitions of this term are in use. The American Society of Heating Refrigeration and Air conditioning Engineers (ASHRAE) state that “Thermal Comfort” is “the condition of mind that expresses satisfaction with the thermal environment” [8]. Hensen defined it as

“a state in which there are no driving impulses to correct the environment by the behavior” [9]. These definitions indicate that the thermal comfort represent a state of mind; thus, it can be affected by the compounding interplay of individuals’ physical and psychological preference, environmental conditions and other factors [10]. This fact means that nobody can provide an absolute standard for assessing thermal comfort.

Generally, an individual feels comfort when arrangement to the environment condition needs minimum physiological effort, the body temperature kept almost constant in a limited range, and the moisture level of skin is low [11]. Studies show that generally, people spend between 1 to 10 hours inside vehicles every day [12]. Therefore, the thermal comfort in vehicles gains more attention these days, and mobile HVAC systems and their ability to provide desired comfort inside vehicles are of special importance.

1.2 Literature Review

Thermal Comfort in Vehicle Cabins

The importance of thermal comfort in buildings is well established, and it is increasingly being applied for the interior of transport vehicles. For instance, in automobiles, it plays an essential role in protecting passengers and controlling their behavior because it associated with decreasing the driver stress level, improving their ability to concentrate, and providing good visibility by avoiding the windshield fog [13][14]. Evidence suggests that establishing thermal comfort at a reasonable cost is among the most critical factors for modern vehicle design. Addressing all the parameters known to affect cabin comforts, such as relative humidity, pressure, air velocity, air temperature, and passengers’ metabolic rate [10] will affect the amount of fuel consumed by vehicles. In fact, the role of AC in the vehicle’s energy

use is undeniable [15]. Annually, cooling systems in automobiles use about 26 billion liters of fuel in the United States [16]. Moreover, increasing tailpipe emissions and consequently, the rise in CO and NO_x are also associated with vehicle air conditioning systems [17]. It should be noted that the portion of CO₂ emissions associated with transportation is about 22% of the total, which will have a substantial impact on global warming [18][19]. Following possible approaches such as decreasing solar radiation loads, developing climatic control systems, and enhancing AC systems can significantly affect the fuel consumption reduction and thermal comfort level within vehicles. However, the importance of global warming is driving to reduce usage and emissions further. Therefore, the auto industry wants to improve AC systems to achieve these goals [20].

In the Hybrid Electric vehicles and Electric Vehicles industries, AC systems have attracted a lot of attention due to their high-power consumption [15][21]. The possibility of decreasing power consumption of electrical and battery-powered vehicles including recreational vehicles (RV) up to 50% by improving their AC systems' efficiency [15][22] means that optimization of AC systems will bring about higher efficiency for electrical vehicles on the road as well as having environmental and economical benefits for industry. Moreover, the ever-increasing cost of energy is among the main motivations of looking into the optimization of the energy systems in all vehicles.

The state in which an individual will feel well, and there is no extra physiological effort for further adjustment to the environment condition represent the definition of thermal comfort. Studies show that “the human thermoregulatory system is quite efficient and tends primarily to ensure thermal equilibrium without an explicit effort and then adjust its reaction to external stimuli” [23]. Based on these definitions, a thermally comfort condition belongs to the environment in which the temperature of body (36.7°C) is preserved with no significant thermoregulation attempt by the human body.

The complexity of thermal comfort assessment in the vehicle cabin environment is due to the rapid thermal transition over time. Moreover, aforesaid projections are more complicated due to erratic thermal environment affiliated with high airspeed around vehicle cabin, heat flux from surrounding surfaces exposed to ambient conditions, and solar radiation [24][25]. Additionally, other effective factors such as transient thermal condition of the prevailing climate inside the cabin, metabolic rates which is dependent on passengers physiological and psychological states, the nonuniform air velocity and temperature distribution due to complications of the internal geometries, the sun irradiance effects and different heat absorption of materials associated with their various absorption capacities, the angles of solar irradiance occurrence, the type of passengers clothes, and their dependent anonymous relationships [11] lead to the complexity of thermal comfort modeling effort for vehicle in-cabin environments. Considering the aforementioned complexities of determination and examination of thermal comfort level in an environment, providing an appropriate analyzing tool can lead future designers in the preliminary steps of vehicle designs and will result in a significant saving in cost and time.

In recreational vehicles (RV), the aforementioned complexities are more pronounced due to the nature of this type of vehicle. RVs bridge the gap between building and vehicle environments, which makes them much more challenging to analyze because they can be treated as neither vehicles nor buildings. For example, similar to a car, they are exposed to an erratic thermal environment adopted from airspeed around the cabin due to the vehicle's movement, the heat flux from the sun, and the ambient conditions. Also, as they are representing a small mobile building where people spend more time compared to a traditional vehicle, evaluating thermal comfort within their cabin is among the essential criteria in the preliminary stages of design. Additional complexities are introduced into the design process due to the existence of multiple appliances, including a stove inside

RVs, which has a notable impact on the inside temperature. Due to the larger size of RVs compared to traditional vehicles, combined with the fact that they contain additional appliances, RVs are much more energy-intensive and require more attention in the design stages to better address battery-management and energy efficiency measures.

Numerous amounts of research and experiments introduce various prediction methods for measuring the thermal discomfort degree of individuals who are subjected to a thermally equivalent environment under steady-state conditions. Nonetheless, studies shown considering steady-state conditions even in buildings are not realistic and practical. Also, the previously mentioned standards are mainly prepared for buildings, and they are not suitable for measuring thermal comfort in vehicles with all the former complexities beside the transient localized ambient conditions in high-speed air velocities.

Considering the limitation of the standards mentioned above as well as the vehicular in-cabin transient environment, using these standards cannot lead researchers to decisive results. As an alternative approach, EN ISO 14505 (The International Organization for Standardization) [26][27][28] are usable for recognizing vehicular thermal comfort. The standard has three parts: 1. Principles and methods for assessment of thermal stress [26]; 2. Determination of equivalent temperature [27]; 3. Evaluation of thermal comfort using human subjects [28]. In these standards, the propounded indices for evaluating thermal comfort are as follow:

- PMV (Predicted Mean Vote) [26],
- PPD (Predicted Percentage of Dissatisfied) [26],
- T_{eq} (equivalent temperature) [27].
- TSV (Thermal Sensation Vote) [28],

Among all these indices, PMV and PPD are useful for assessing thermal comfort inside homogeneous environments in buildings under steady-state conditions. The other indicator is the equivalent temperature, which is a local index for analyzing thermal discomfort. The last indicator, TSV, is used in a subjective methodology in which individuals' feed-backs about their thermal feeling in an environment are documented and investigated.

Generally, the equivalent temperature (T_{eq}) method has a lower sensitivity to cold environments parameters compared to the warm ones [29]. On the other hand, the TSV method is more appropriate only for those situations in which a small amount of the total body heat transfer is generated by the latent evaporation heat. Paul Danca et al. [30] also show the insufficiency of the PMV model for segregating the vehicle cabin's environment. Compared to normal conditions within a vehicle compartment, the airspeed in the standard is assumed to be very low; therefore, the PMV method can not lead to realistic results. On the other hand, some other factors exist that can affect thermal sensations unpredictably, such as heat conduction through seat covers, which are not considered in those standards [31][32][33]. Moreover, according to experimental subjective researches, the calculated comfort level by using standards' suggested methods can be significantly different from the actual passengers' thermal state feelings records [30].

In the current study, the temperature distribution is modeled for the evaluation of thermal comfort in a vehicle compartment. Temperature is among the main factors when designing for thermal comfort. Moreover, it is the easiest factor to control through heating/cooling within the space, and the temperature gradient within the space can be controlled through fans that induce air circulation. Other factors such as clothing factor (clo) and metabolic rates are also important when designing for thermal comfort; however, they are related to temperature and relative humidity, and it is not possible to design a space around those factors, as the idea of "average occupant" does not apply to these concepts.

It is also possible to control relative humidity through rigorous design for specific buildings such as museums; this can be done through the use of humidifiers and dehumidifiers since variables such as infiltration rate, location, climate, and building enclosure details are known. This does not apply to vehicles, as most of these variables are unknown and cannot be controlled from a design perspective. Also, the majority of vehicles do not have dedicated humidifiers and dehumidifiers within them to control relative humidity to thermally-comfortable levels. Additional factors, such as opening the windows, also completely change the quantity of moisture within the vehicle. Last but not least, the location where the vehicle is being used has a direct impact on the relative humidity within vehicles, and it is not possible to generalize the results for all possible locations. Other factors such as occupant behaviour, the type of food being cooked and the number of occupants inside the vehicle directly impact the relative humidity within the RV. The combination of these factors makes it complicated to create a reliable model to control the relative humidity within vehicles accurately; hence, the main focus will be placed on temperature and air velocity, as it can be controlled through heating/cooling systems within most cars and the study of the relative humidity effect will be considered as the future work of the current research.

State-of-the-art in thermal comfort prediction

It is possible to assess the cabin thermal comfort using various approaches, such as experimental methods, low-order models, numerical simulation, etc. Each of these approaches will briefly be covered in this section, along with their limitations.

- Experimental and theoretical models:

A combination of theoretical and experimental approaches is usually used by re-

searchers. Kaynakli et al.[34] used a theoretical method to evaluate the interactions between the human body and an interior domain under steady-state conditions. A combination of theoretical and experimental research was performed by Kaynakli and Kilic to study the thermal comfort inside the vehicle cabin during heating time [35]. An investigation of room geometry's effect on the average temperature was done by Kalmar and Kalmar [36]. Liu et al.[37] compared experimental data of measured skin temperature with calculated values by theoretical methods. Barna and Banhidi [38] experimentally study the effect of warm floors and the radiant temperature with a thermal manikin in a climate chamber. Alfano et al.[39] reproduced the typical microclimatic conditions in a test-room in order to investigate temperature measurement methodologies with considering metrological performances and pragmatic assumptions. Arslanoglu and Yigit [40] compared experimental measurements and theoretical methodology to assess the effect of radiation heat flux on human body thermal comfort.

- Low-Order Models:

A multiplicity of scientific approaches can be used for the modeling of complex, non-linear systems. Of the main approaches, we note energy-based mathematical models, lumped-parameter models, black-box modeling, and grey-box modeling; the approaches and their shortcomings are summarized in [41] and [42]. Reduced-order models for thermal analysis have been used extensively in home interior energy balances [43][44], as well as for energetically demanding closed-systems such as data centres [45][46]. These models have been coupled to optimization software with imposed constraints, to explore the parameter space of the system [44]. Recent works by the National Renewable Energy Laboratory in the United States have developed stand-alone thermal management models for vehicular interior climate analysis. These

tools, primarily focused on Class 8 Truck cab, have been central to the 35.7% reduction of the air-conditioning load and a 43% reduction in the heating load. These changes were tributary to the use of specific insulation with a reflective radiant barrier as well as the optimal consideration of window shades and paints [47]. The development of these thermal modeling tools takes inspiration from electrical engineering and is integrated within the Matlab/Simulink framework [48]. Most of these studies rest on a solid understanding of automotive air conditioning, the state-of-the-art in this field is summarized in a recent book [49].

- Numerical models:

Many researchers have used CFD (Computational Fluid Dynamics) simulations to analyze different factors that contribute to thermal comfort in buildings. Sørensen and Voigt used CFD simulations for modeling a seated human in a room, subjected to convective and radiative heat transfer [50]. Salmanzadeh et al. took a similar approach, but focused on using CFD to look at the buoyancy-driven thermal plume around a heated mannequin [51]. Others have put more emphasis on the air movement in their CFD analyses. For example, another study by Abdelmaksoud and Khalil looked at different ventilation CFD cases in an office and showed that up to 30% reduction in cooling energy could be achieved while maintaining an acceptable thermal comfort level to the occupants [52]. A similar study by Yongson et al. investigated the impact of the position for an air-conditioner blower on the temperature and air velocity distributions within a room to help select the best location to maximize thermal comfort [53].

The concept of thermal comfort is not limited to buildings, and many researchers have used CFD simulations to investigate the thermal comfort within vehicles. Fu-

jita and Nakagawa used CFD analysis to evaluate the thermal conditions in a car while accounting for radiative, conductive, and convection heat transfer [54]. Numerous studies by several researchers have focused on assessing the impact of outside conditions, such as solar radiation, temperature, etc. on the conditions within the vehicle, which are directly tied to thermal comfort inside vehicles [55][56][57][58][59]. To simplify the CFD approach, Ye [60] developed a correlation procedure of the simplified CFD cabin model using physical test results to provide a practical method for addressing current design needs. Clearly, thermal comfort within vehicles is sophisticated and is affected by many external variables, which make it a difficult subject to study.

There is no doubt that investigating thermal comfort and defining the relationship between potential parameters necessitates a lot of experiments. In the experimental method, taking temperature and humidity measurements at multiple locations and at different times would be costly and difficult to repeat unless a dedicated controlled chamber is constructed. Therefore, the total cost of the study can enhance significantly by setting up experiments. On the other hand, it is easier to use software such as MATLAB's Simulink, which assumes repeatable conditions, but as a result, it is unrealistic due to low accuracy. The low-order models are not practical tools for optimization since the model is not true physics. Furthermore, these models require a lot of experiments to be verified, developed, and revised.

As technologies grow up, more intricate problems appeared, which required a more flexible, faster, and cheaper methodology for further investigation, especially for complex geometries. Hence, computational fluid dynamics gain immense popularity due to its ability to prepare diverse and detailed predictions about airflow patterns and thermal comfort. Compared to experimental approaches, numerical simulation is less expensive and is ca-

pable of evaluating the airflow field in a short period. Furthermore, CFD can be a usable tool for providing virtual distribution of temperature, humidity, and airflow in the space, which is very costly and time-consuming by experiments. Additionally, CFD is capable of giving transient simulations under various procedures and is usable for optimization of air circulation within the domain.

All the aforementioned capabilities put CFD on the center of attention, among other methods, and make it an easier tool for thermal comfort design. However, the dependency of numerical methods on grid distribution, model selection, and many other factors will increase the uncertainty of this approach while facing complex problems. Thus, there is still a tendency toward combining numerical methods with experimental approaches, which means using computational fluid dynamics may not take over experimental works thoroughly.

1.2.1 Motivation

Thermal comfort is of particular importance in the vehicle compartment due to its crucial influence on reaction time, protecting passengers, and controlling their behaviors. For a sustainable design approach toward mobile HVAC systems, the analysis of dependency of thermal comfort and HVAC energy usage is required. Any improvement in HVAC system performance is potentially coupled with the thermal comfort inside the vehicle, as well as a noticeable decrease of greenhouse gas emissions and the overall energy utilization. Careful analysis and optimization of temperature distribution pattern within the compartment domain are required for an efficient operation of vehicular HVAC system and a proper design. This procedure will consist of: i) a detailed study of the space features including air distribution, wall properties, and opening, ii) appropriate design of the interior spaces

for more active and efficient air circulation.

Active climate control of interior spaces is an essential feature of the occupants' thermal comfort. A temperature correction, either by active cooling or heating, requires an input of energy to the system. The need to provide a comfortable interior space is often balanced by the energetic demands on the system. The energetic demands are especially important in the RV industry as the RVs are equipped with large batteries to operate their electrical systems while off the grid. Optimal battery usage can be achieved through a careful reconsideration of the thermal components of the system. By abstracting the interior of an RV as a coupled thermo-fluid control volume with thermal sources with exchanges occurring through the boundaries, the overall system behavior can be better understood and optimized. Ultimately, a better understanding of the coupled behavior of the system will inform the thermal design of the RVs, which can increase the duration of the grid independence in this product.

1.2.2 Objectives

The overarching objective of this thesis is to use CFD for assessing thermal comfort in a class B recreational vehicle's interior and optimizing thermal distribution within the compartment based on a parametric study. This is essential because currently, optimizing thermal distribution does not receive enough attention at the preliminary design stages. This is done using ANSYS Fluent software package. Optimizing airflow and temperature distribution patterns which depends on different factors such as interior space design, air velocity, velocity direction, heat fluxes through various components, etc. will directly guide designers toward achieving suitable thermal comfort level in cabins. The ability of the numerical method to provide the virtual perspective of temperature distribution within

the RV cabin pursues the goal of improving thermal comfort.

1.2.3 Thesis Structure

Detailed investigation of the relevant literature shows that CFD can be used for thermal comfort evaluation. Therefore, this study plans to use CFD for further investigation of temperature distribution and thermal comfort in an RV. Chapter 2 covers the numerical tools and verification cases. In section 2.1, key parameters in numerical modeling, including turbulence model and grid discretization, are introduced. Section 2.2 is devoted to presenting a validation of a numerical simulation of natural convection. In this section, experimental data of temperature distribution of a cubical room with natural convection are used for verifying numerically simulated case in ANSYS FLUENT software. This verification is necessary to show that CFD can reproduce the room environment similar to experimental measurements; thus, CFD can be a practical tool for further estimation of temperature distribution.

In chapter 3, the RV geometry is built in ANSYS FLUENT software. More details about the problem definition, mesh generation, boundary conditions, and turbulence model selection are described in section 3.1. Furthermore, the results of the CFD simulations of the existing RV are presented in section 3.2. This part is followed by a parametric study. In the parametric study, the impact of inlet and outlet vent locations, supply airflow direction, and varying the number of exhaust vents on temperature and airflow distribution are investigated. At the end, the most optimal and efficient case is selected based on having the best distribution of air and temperature.

In chapter 4, the major contributions of this thesis are concluded and it is followed by suggestions for future studies.

Chapter 2

Numerical Method and Validation Case

Prior to the investigation of the results, it is imperative to cover the concepts required to understand CFD simulations. This means that the basic terminology, the approach used for defining problems, and the selections for appropriate solvers must be explained. Section 2.1 provides some of the details to clarify the numerical modeling used henceforth.

Next, a validation case will be investigated to explore the accuracy of the applied CFD model. For this purpose, domain discretization and boundary conditions are discussed, and it is followed by a comparison of the CFD simulations with the experimental data.

2.1 Numerical Modeling

Computational Fluid Dynamics (CFD) is the science producing quantitative predictions and analysis of fluid motion by solving the equations of fluid flow numerically. The possibility of doing a detailed analysis of complex cases is one of the main motivations for using CFD. These models are favorable when the experimental methods are time-consuming or

when an excellent resolution of airflow is needed for studying the impact of parameters related to fluid dynamic problems. In order to numerically solve a fluid dynamic problem, multiple partial differential equations have to be solved simultaneously; these equations include the conservation of mass, momentum, and energy. The general methods in use are finite volume, finite element, and finite difference methods. Computational grid, boundary conditions, and initial conditions are also effective in this procedure.

After dividing the geometry into small grids and defining boundary conditions, the Navier-Stokes equations are solved for each cell of the entire domain. It should be taken into account that the selection of the proper method for discretization and time-marching may vary from case to case based on the fluid condition.

2.1.1 Governing Equations

Reynolds Averaged Navier-Stokes (RANS) equations governing the fluid flow are given in Eq (2.1) , Eq (2.2), and Eq (2.3) [61]:

Continuity:

$$\frac{\partial \bar{\rho}}{\partial t} + \nabla \cdot (\bar{\rho} \tilde{U}) = 0 \quad (2.1)$$

Reynolds equations:

$$\frac{\partial \bar{\rho} \tilde{U}}{\partial t} + \nabla \cdot (\bar{\rho} \tilde{U} \tilde{\mathbf{U}}) = -\frac{\partial \bar{P}}{\partial x} + \nabla \cdot (\mu \text{ grad } \tilde{U}) + \left[-\frac{\partial (\bar{\rho} u'^2)}{\partial x} - \frac{\partial (\bar{\rho} u' v')}{\partial y} - \frac{\partial (\bar{\rho} u' w')}{\partial z} \right] \quad (2.2a)$$

$$\frac{\partial \bar{\rho} \tilde{V}}{\partial t} + \nabla \cdot (\bar{\rho} \tilde{V} \tilde{\mathbf{U}}) = -\frac{\partial \bar{P}}{\partial y} + \nabla \cdot (\mu \text{ grad } \tilde{U}) + \left[-\frac{\partial (\bar{\rho} u' v')}{\partial x} - \frac{\partial (\bar{\rho} v'^2)}{\partial y} - \frac{\partial (\bar{\rho} v' w')}{\partial z} \right] \quad (2.2b)$$

$$\frac{\partial \bar{\rho} \tilde{W}}{\partial t} + \nabla \cdot (\bar{\rho} \tilde{W} \tilde{\mathbf{U}}) = -\frac{\partial \bar{P}}{\partial z} + \nabla \cdot (\mu \text{ grad } \tilde{W}) + \left[-\frac{\partial (\bar{\rho} u' w')}{\partial x} - \frac{\partial (\bar{\rho} v' w')}{\partial y} - \frac{\partial (\bar{\rho} w'^2)}{\partial z} \right] \quad (2.2c)$$

Scalar transport equation:

$$\frac{\partial \bar{\rho} \tilde{\Phi}}{\partial t} + \nabla \cdot (\bar{\rho} \tilde{\Phi} \tilde{\mathbf{U}}) = \nabla \cdot (\Gamma_\Phi \text{ grad } \tilde{\Phi}) + \left[-\frac{\partial (\bar{\rho} u' \varphi')}{\partial x} - \frac{\partial (\bar{\rho} v' \varphi')}{\partial y} - \frac{\partial (\bar{\rho} w' \varphi')}{\partial z} \right] \quad (2.3)$$

Where \tilde{U} , \tilde{V} , and \tilde{W} are the Favre-averaged velocity components, u' , v' , and w' are the fluctuating velocity components, $\bar{\rho}$ is the time-averaged fluid density, P is the pressure, μ is dynamic viscosity of fluid, t is time, $\tilde{\Phi}$ is the Favre-averaged of flow property, $'$ is the fluctuating component of flow property, and Γ_Φ is molecular diffusion coefficient.

In flow and heat transfer calculations, it is assumed that the fluid is single phase and variable density incompressible, while being subjected to the gravitational field with a constant viscosity in order to simplify the numerical investigation.

2.1.2 Turbulence modeling

One of the most prominent characteristics of airflow is turbulence. For turbulent flow, velocity, pressure, and other physical parameters change very fast, and this leads to a

growing dispersion in the momentum and energy. It is vital to select an appropriate turbulence model as it has a direct impact on the accuracy and the time it takes to perform each simulation; hence, an acceptable compromise has to be made to produce results that are deemed accurate enough. Among the turbulence models, Re-Normalization Group $k-\epsilon$ model (RNG) is one of the best for modelling indoor environments [62][63][30]. In the following paragraph, the most important features of the RNG $k-\epsilon$ model are briefly described.

In general, the most common features of $k-\epsilon$ models are the robustness, computational efficiency, and reasonable accuracy for modeling various turbulent flows. The determinative variables in these models are the turbulence kinetic energy (k) and dissipation rate (ϵ). Among different types of $k-\epsilon$ models, the RNG $k-\epsilon$ model indicates better results for complex flows and enhanced predictions of both incompressible [64] and compressible flows [65]. In RNG $k-\epsilon$ model, Navier-Stokes equations are renormalized to account for all scales of motions which contribute to the turbulent dispersion, while in the standard $k-\epsilon$ model, the turbulent diffusion is only calculated for a single length scale. In RNG $k - \epsilon$ model, two modifications are implemented: two new equations for calculating the turbulent viscosity term and the dissipation rate (ϵ). These modifications are applied to eliminate the accuracy limitations of the standard version of the $k - \epsilon$ model [61]. Therefore, the results provided by RNG model are more realistic. Furthermore, in predicting incompressible turbulent flows, RNG $k-\epsilon$ model has significant improvement over standard $k-\epsilon$ model for recirculating flows such as for cases of backward-facing step, as well as shear flows such as for confined co-flow jets [66]. Due to these features and the ability of this model for simulating indoor environments, it is chosen for the current study. The applicability of this model will be examined in the next section by comparing the simulation results to existing experimental measurements taken from within a conditioned space. Additional informa-

tion about other turbulence models available in the literature can be found in Table 2.1 which were taken directly from Danca 2018 [1].

Table 2.1: Disadvantages and advantages of different turbulent models [1].

Model	Advantages	Disadvantages
Spalart Allmaras	Low time consuming-1 equation;	Not Suitable for many cases;
$k - \epsilon$ standard	Robust, economic, reasonable accuracy;	Weak results for complex flows; errors for special cases like boundary-layer, jet;
$k - \epsilon$ RNG	Indicated for medium to complex flows, enhanced predictions of recirculating and shear incompressible flows such as confined co-flow jets;	parameter-dependent solution, errors on boundary-layer;
$k - \epsilon$ realizable	same benefits and additional near wall treatment;	Limitations due to turbulent viscosity isotropicity hypothesis;
$k - \omega$ standard	Applicable for flows around obstacles and boundary layer flows; For airflows interior buildings- good accuracy and numerical stability [67];	Sensible to correct boundary layer conditions for turbulence [67];
$k - \omega$ SST	$k - \omega$ std model's accuracy near walls and $k - \epsilon$ model's independency for free flows;	It is necessary to have a very fine mesh for the boundary layer;
laminar	Not applicable for the airflows considered in the studied cases; (Reynolds numbers are in the turbulent regime)	

2.1.3 Boundary Conditions

One of the steps in defining a fluid dynamic problem is identifying proper boundary conditions and initial conditions. Boundary conditions can be categorized into three general groups:

- Dirichlet boundary conditions
- Neumann Boundary conditions
- Mixed boundary conditions

The Dirichlet boundary condition refers to having a constant value at the given boundary. In terms of the simulations done in this study, this would correspond to a constant wall temperature. For example, if there are any isothermal (insulated) boundaries, they can be categorized as Dirichlet boundary conditions with a constant temperature. As will be presented in the validation section, previous studies have used constant wall temperatures as their boundary conditions; hence, a similar approach will be taken in this study.

On the other hand, the Neumann boundary condition refers to having a known derivative function at a given boundary. Heat fluxes applied to walls are an example of this type of boundary condition.

In a mixed boundary condition, a combination of the aforementioned boundary conditions is used for defining the boundary settings. An example of this would be when multiple heat transfer modes are occurring simultaneously, and the boundary condition can neither be treated as a constant temperature, nor a known heat flux, but a combination of the two.

2.1.4 Mesh Generation

Mesh generation consists of discretizing a volume into a finite number of small elements over which the governing equations will be solved. These elements are small simple shapes such as tetrahedral, pyramid, prism, or hexahedral in three dimensions simulations (Figure 2.1). A mesh can be structured or unstructured with regards to each element's relation to its neighbors. The disadvantage of unstructured mesh is that there is more tendency toward numerical errors; moreover, more memory is needed to store the mesh and the relational database between the mesh elements. On the other hand, structured mesh leads to easier programming and reduced computational costs due to more effortless connectivity of the elements and data management. Nevertheless, poor adaptability to complex geometries is considered as the main disadvantage of structured mesh. In the current study, a structured mesh is used for validation case, and unstructured mesh is used for the main numerical simulations.

Generally, the higher the number of elements, the higher the accuracy in the results, this comes at the expense of more computing time. But it should be taken into consideration that at some point, increasing the number of elements does not affect nor improve the results. This means the simulation is not dependent on the mesh anymore.

2.1.5 Boundary Layer

To adequately resolve the boundary layer, wall scaling is introduced, known as y^+ . y^+ is defined as the distance from the wall and it is a dimensionless quantity for investigating the applicability of wall functions. This term can be denoted by Eq 2.4:

$$y^+ = \frac{yu_\tau}{\nu} \quad (2.4)$$

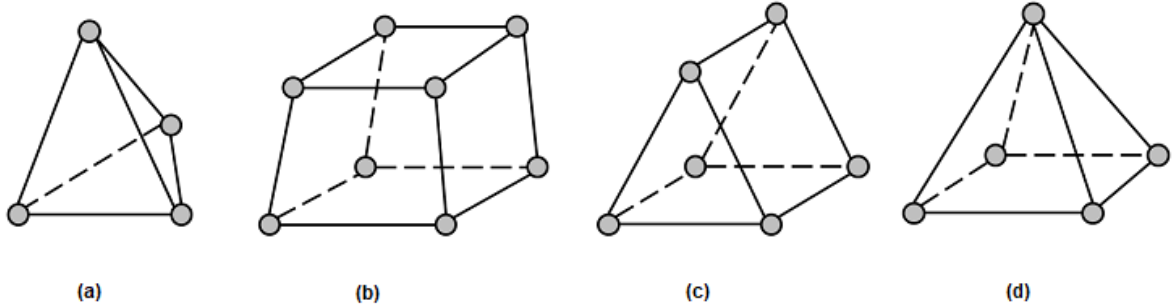


Figure 2.1: Element Shapes in 3D meshes, a) tetrahedral b) hexahedron c) prism d) pyramid [5]

Where u_τ is the friction velocity, y is the absolute distance from the wall, and ν is the kinematic viscosity. The friction velocity can be calculated by Eq 2.5:

$$u_\tau = \sqrt{\frac{\tau_\omega}{\rho}} \quad (2.5)$$

with

$$\tau_\omega = \mu \frac{du}{dy} \quad (2.6)$$

Where τ_ω is wall shear stress, ρ is the flow density, and $\frac{du}{dy}$ is the gradient defined at the wall. y^+ can have different values with regards to different wall functions associated with different turbulence models. Three regions are defined for the flow based on y^+ values. These regions are as follows:

1. The viscous sublayer region ($y^+ < 5$):

The characteristic feature of the viscous layer is that the Reynolds shear stress can be neglected due to the domination of fluid by the viscous effect. The velocity profiles are given by Eq 2.7:

$$u^+ = y^+ \quad (2.7)$$

2. The logarithmic region ($y^+ > 30$):

The feature of this layer is that the turbulence shear stress predominates. In this layer, the velocity profile changes by a logarithmic function along y . The velocity profile in this region can be defined by Eq 2.8:

$$u^+ = \frac{1}{\kappa} \ln(y^+) + B \quad (2.8)$$

Where κ is the Karman constant with value of 0.41 and B is a constant value of 5.2.

3. The buffer layer ($5 < y^+ < 30$):

The feature of the buffer layer is that both the viscous and turbulent shear dominate and due to the complexity of this layer, the velocity profile is hard to be defined. This layer can be defined through asymptotic theory based on near-wall and log-layers.

Generally, to have reliable results from the simulation, y^+ should be smaller than 5 for wall resolving.

2.2 Validation Case

Investigating the temperature distribution is imperative for improving thermal comfort in buildings. Heating systems, people, and electronic appliances are the effective heat sources which play an important role in generating air circulation and temperature stratification within a space. In the absence of forced convection, the temperature distribution caused by the heat sources leads to buoyancy-driven air circulation within the area. In a mechanical ventilation system, this phenomenon can be exploited by adjusting the locations for the inlet and outlet vents in the space to promote better mixing. This is the basis of Displacement Ventilation in HVAC.

The temperature distribution can be investigated experimentally, analytically, or using numerical methods, each of which has its own pros and cons. For example, experimental measurements can provide real data, but it could be complicated and costly to instrument given space to take a large number of measurement points [68][69][70]. On the other hand, analytical methods are developed for simplified cases, which cannot be directly used in complicated problems with complex geometries and conditions. As for numerical methods, CFD can provide a full-scale study of flow field within a given space. However, the accuracy and reliability of the CFD models are not well-established yet, and validation and verification of CFD models are required. Moreover, the inconsistency of turbulence models' performances in simulations makes it difficult for defining a fixed model for a specific subject. For example, in some studies, the RNG $k-\epsilon$ model is applied [71][72][73][74][75][76][77], while many others use the SST (Shear Stress Transport) $k-$ model in their simulations [78][79][80][81]. Considering the advantages and disadvantages of different methods, researchers mostly prefer to predict indoor air quality by using CFD.

The intent of this section is to evaluate the temperature and airflow pattern inside a room with two vents and one heat source. To do so, experimentally measured air temperature data from Li et al. [82][2] are used for validating the numerical simulation. The details about the experimental setup used by Li are provided in the first sub-section. The second subsection presents the computational procedure and the boundary conditions defined with regards to the experiments. The results and the discussion are presented in the following subsection.

2.2.1 Experiment Set-up

Among all different cases that were investigated by Li [2], case B1 is selected for the current study because more details and justifications of modeling choices were available for this case. Figure 2.2 shows a schematic of the test room. The width, length, and height of the test room were $3.6m$, $4.2m$, $2.75m$, respectively, as shown in the figure. The interior walls were painted black. The heat transfer coefficients for the walls, the ceiling, and the floor are all $0.36 \frac{W}{m^2 K}$, except for wall 4, which is assigned a value of $0.15 \frac{W}{m^2 K}$. The inlet and outlet dimensions are $0.45m \times 0.5m$ and $0.525m \times 0.220m$, respectively. The effective area for the perforated inlet grille was $0.1125 m^2$. The inlet (T_i) and outlet air temperatures (T_o) were $16^\circ C$ and $27.3^\circ C$, respectively. A heat source with a porous surface was located at height $Y = 0.1m$ and $X = 2.7m$ far from the inlet. It includes 25 light bulbs and could provide up to $600W$ of heat. In the current case, the heat load was set as $300W$. For measuring the room temperature, 54 thermocouples were set up at different locations, including a vertical pole in the test chamber, the interior surfaces, inlet, and the outlet vent.

2.2.2 CFD Simulation Set-up

In this section, the details about the numerical simulation are described.

Grid Discretization

The geometry is discretized into 1.9×10^6 hexahedral elements. Figure 2.3 shows the generated mesh. The distance from the wall-adjacent cell to the wall is $0.0002m$, which leads to $y^+ = 0.8$ for defining the viscous sub-layer.

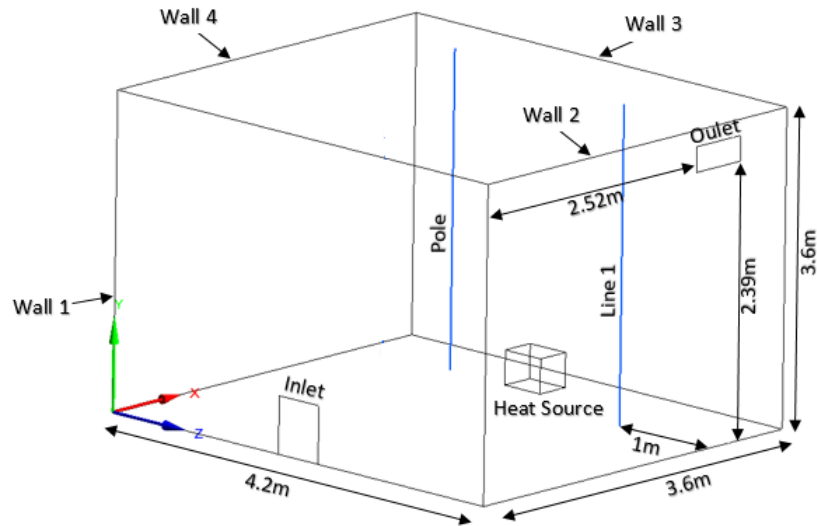


Figure 2.2: Geometry of Room.

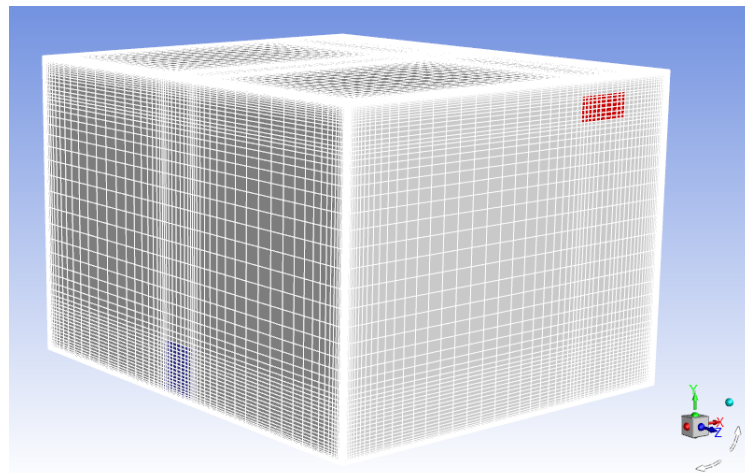


Figure 2.3: Grid discretization of the test room geometry.

Boundary Conditions

The heat source is defined with a constant heat flux through surfaces of the heat source ($q = 454.5 W/m^2$) calculated as:

$$q = \frac{E}{A_{hs}} \quad (2.9)$$

Where A_{hs} is the heat source surface area in m^2 and E is the heat load in W .

The outlet to the room is defined as having zero static pressure with $T_o = 27.3^\circ C$. The air flow is supplied to the room with a constant velocity of $u = 0.0513 \frac{m}{s}$ and temperature of $T_i = 16^\circ C$. The air is considered incompressible and its properties are selected at $24.5^\circ C$ which is the average temperature along the vertical pole. The following values are determined for air properties: operating pressure $101,325 Pa$, density $1.17 \frac{kg}{m^3}$, thermal expansion coefficient $0.003 \frac{1}{K}$, thermal conductivity $0.026 \frac{W}{mK}$, characteristic length $2.75 m$, dynamic viscosity $1.8310^{-5} \frac{kg}{ms}$, and specific heat capacity $1006.95 \frac{J}{kgK}$.

For the wall surfaces, a fixed temperature condition is implemented. Table 2.2 shows the wall exterior temperatures based on measured data [2]. In Li's study, temperature measurements were not taken for the ceiling and the floor; hence, the temperature of the zone just above the floor ($22.4^\circ C$) and the temperature of the zone just below the ceiling ($24.4^\circ C$) are set as the boundary conditions of these surfaces.

Table 2.2: Exterior Walls' Temperatures [2].

Location	Wall 1	Wall 2	Wall 3	Wall 4	Floor	Ceiling
Temperature($^\circ C$)	20.2	22.7	23	23.2	24	24.2

2.2.3 Solver Settings

ANSYS/Fluent 19.1 is used for this simulation. The RNG $k - \epsilon$ model combined with 3D RANS equations, are solved for this simulation. The steady solution is defined for solving the RANS equations. For Pressure-velocity coupling, the SIMPLE (Semi-Implicit Method for Pressure-Linked Equation) algorithm is used. Second-order discretization schemes are implemented for viscous, pressure, and the convection terms of the equations. The simulation is considered converged when the residuals reach to 10^{-4} .

Results

The results for temperature were compared with experimental data gathered by Li [2] and additional CFD results generated by [83] based on the same experimental data. The CFD and the experimental results along the pole and line 1 are compared shown in Figure 2.4 and 2.5 respectively. In general, these results are in good agreement. It is noted that the CFD results underestimate the temperatures close to the ceiling and the floor, and marginally overestimate the temperature along with the rest of the pole. The differences can be due to assuming a uniform inlet velocity profile and approximating the temperature of the adjacent zones for defining the floor and the ceiling boundary conditions. The air temperature distribution contours are shown in Figure 2.6. Figure 2.6a is depicting an XY plane placed on $Z = 2.1m$, which intersects the inlet and the heat source, while Figure 2.6b is showing a ZY plane located at $X = 2.8m$ which crosses the heat source and the outlet. The buoyancy effect can be distinguished in these figures by the plume-shaped flow created above the heat source. The buoyancy effect is caused by a vertical difference in the air temperature within the zone. Due to this temperature variation, air circulation is created from lower zones to the upper ones. It is also shown that air is captured in

recirculation zones; therefore, the cold air coming from outside through the inlet vent cannot propagate entirely in the room, and consequently, the temperature is high in the upper regions compared to the lower ones.

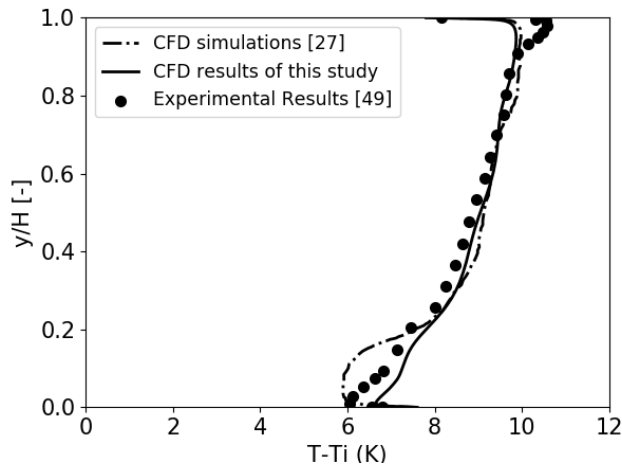


Figure 2.4: Comparison between temperatures at pole.

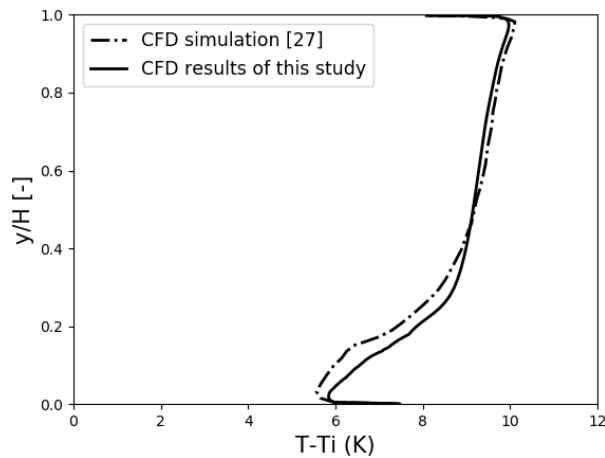
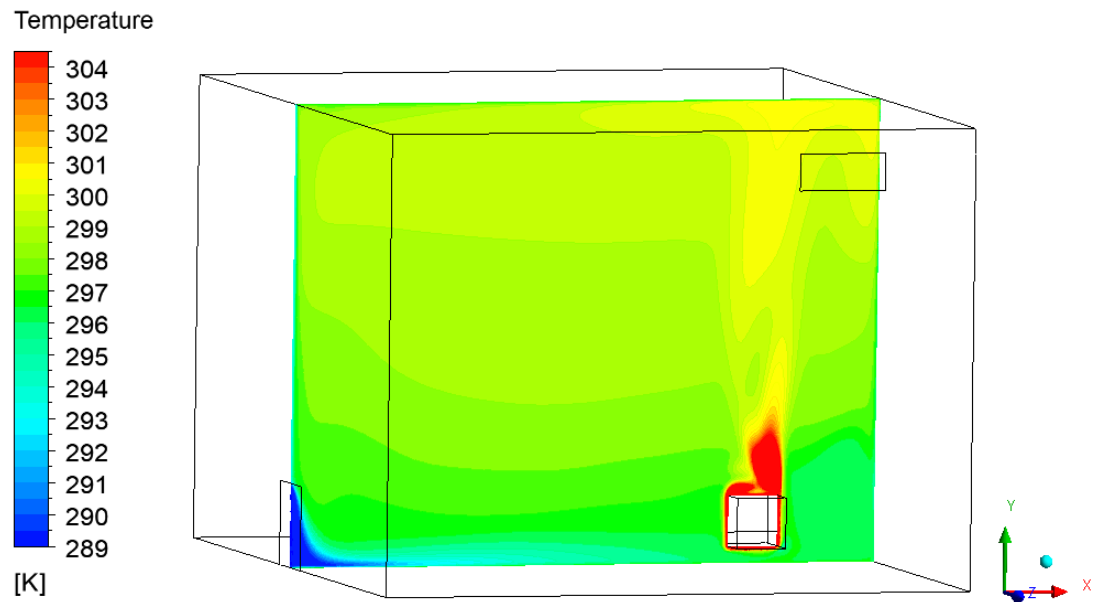
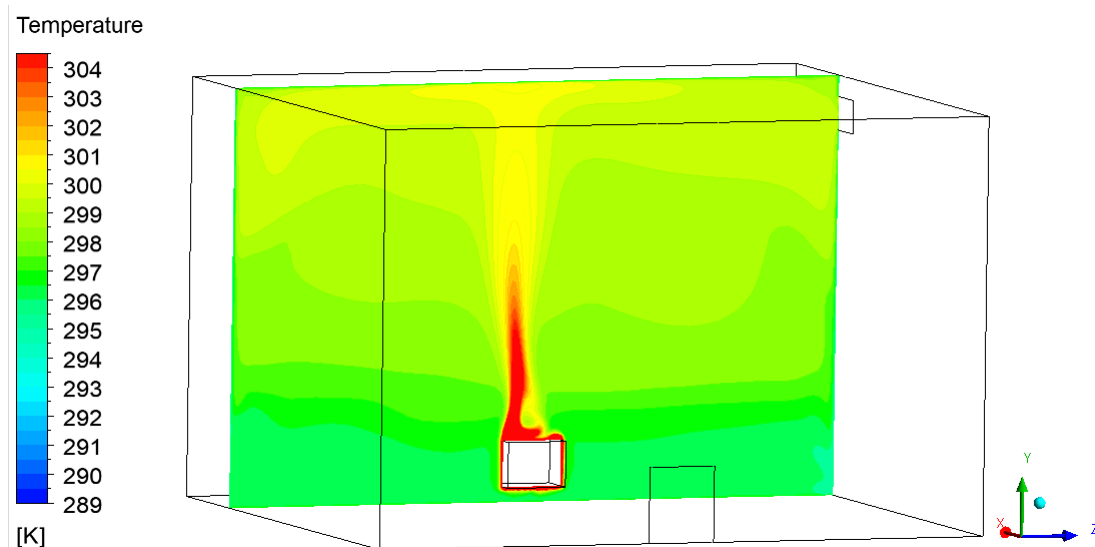


Figure 2.5: Comparison between temperatures at line 1.



(a) at $Z = 2.1m$ (XY plane)



(b) at $X = 2.8m$ (YZ Plane).

Figure 2.6: Distribution of temperature at steady state condition.

Chapter 3

Numerical Simulation of Recreational Vehicle Cabin

In this chapter, the configuration of the reference Recreational Vehicle's (RV) interior environment is defined with appropriate boundary conditions for the model. The model is then used to perform a parametric study to evaluate the optimum case scenario in terms of temperature distribution and thermal comfort within the space.

3.1 Numerical model

3.1.1 Problem Description

Efficient energy usage in battery-powered vehicles such as RV is gaining in importance. The energy usage is an especially important parameter to consider when the systems in the vehicle are in operation but without an electrical source to replenish the battery.

Considering the fact that the air conditioning is among the most energy-consuming systems in RVs, designing an optimized cooling and heating system is an essential principle during the early stages of the design. Airflow pattern modification by active climate control, not only leads to a reduction in energy usage but can also provide a stable thermal comfort condition for the occupants.

A class-B RV is selected for the purpose of this study, namely the Erwin Hymer Aktive. The company's strategy is to purchase a van and make improvements to it. This leaves much room for improvements to be made to address thermal comfort in their vehicles, and this is the main reason why this vehicle was chosen. At first glance, a class-B RV looks similar to a van; this is the reason why they are also called camper vans. These vehicles have suitable heights for an average-height passenger standing upright inside the RV. The cabin has maximum interior dimensions of $width \times length \times height = 2.034 \times 5.045 \times 2.027 \text{ m}^3$. The interior space includes small-size amenities similar to those found in a typical household, such as a kitchen, living room, and a bathroom. Within the RV, heat-generating appliances are used, such as a microwave, fridge, and oven for the kitchen, water-pump for the bathroom, LED (Light Emitting Diode) lights, and TV (television). For thermal comfort consideration, the heat released from these appliances must be accounted for the analysis. All these appliances will be incorporated into the CFD model.

In order to gain a primary understanding of the problem, a simplified numerical model of the RV's interior space is developed. For this study, the physical geometry is based on an Erwin Hymer Aktive RV (Figure 3.1 [84][85]). Figure 3.2 shows the 3D geometry of the RV, including the interior spaces made in ANSYS Space-Claim, which is the ANSYS specific software for creating geometries. In Space-Claim, some complexities of the real model, such as corner fillets, are simplified in order to decrease the computational cost. The goal is to create a representative geometry that is detailed enough to capture the most

important physical flow features. Moreover, extra extrusions representing the locations of TV, power inverter, and water-pump are modified into simple surfaces that produce heat fluxes. Detailed calculations for heat flux estimations will be presented later.

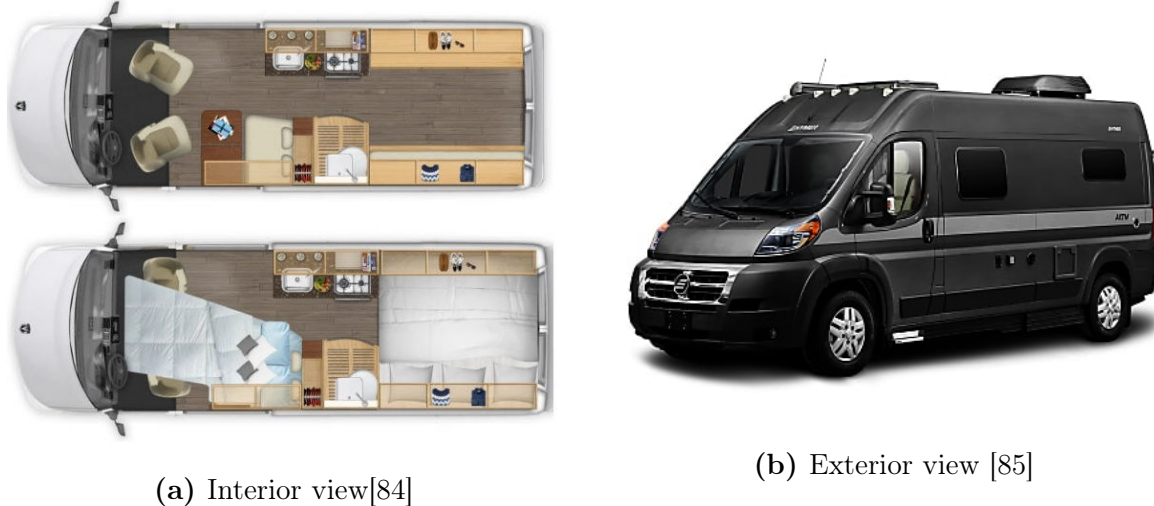
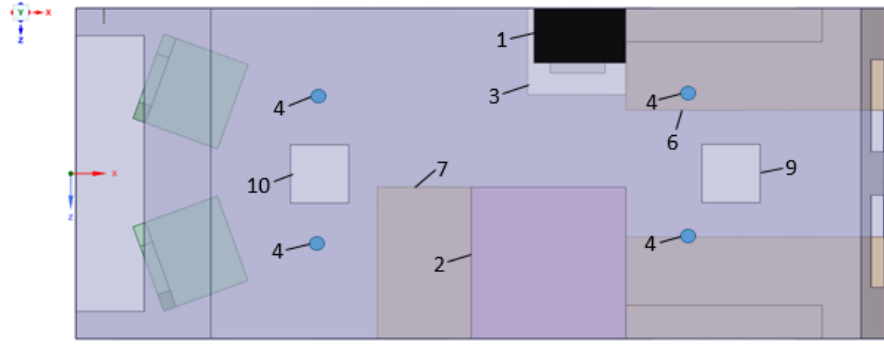
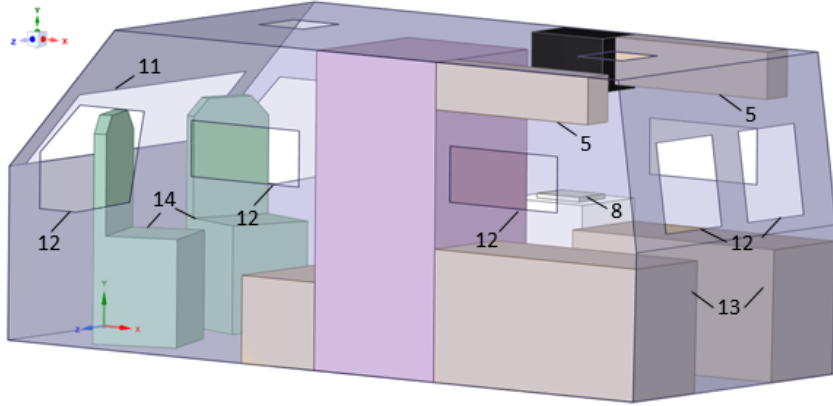


Figure 3.1: Erwin Hymer Aktiv RV Class B.

The location of the AC system is on the roof of the RV, and it supplies air into the cabin through one simple injection grille port at a user-defined relative humidity and temperature. The test RV cabin includes one microwave, one refrigerator, eight LED halogen lights, one power inverter, one water pump, one television, two cabinets, and two boxes simulating two pieces of furniture, which can turn into a twin bed. The placement of all components and appliances, including the supply and exhaust grille locations within the cabin, are also shown in Figure 3.2. These locations are defined by Erwin Hymer's designers.



(a) Top view



(b) Perspective view

Figure 3.2: 3D Geometry of the RV's Inner Space (locations of appliances, inlet, and outlet: 1, microwave; 2, television; 3, refrigerator; 4, lamps; 5, cabinets; 6, inverter fan grille; 7, water pump; 8, oven; 9, AC grille; 10, exhaust grille; 11, windshield; 12, windows; 13, furniture; 14, seats)

3.1.2 Heat Flux Estimations and Boundary Conditions

A fluid-type zone is considered for the in-cabin domain. The appliances and the cabinets are modeled as hollow shells with constant heat fluxes or temperatures imposed at relevant

boundaries. The amount of heat flux generated by each appliance is defined according to Eq 3.1:

$$q = \frac{E}{A_{hs}} \quad (3.1)$$

where E represents each appliances' rated power in Watts (W) and the A_{hs} is the heat-source surface area in square meter (m^2). Based on the conservation of energy, it can be assumed that all electrical and mechanical energy consumed by the appliances is turned into heat load [86]. Admittedly, this provides an overly conservative estimate for the thermal comfort assessment of the vehicle. For example, an electrical appliance such as an electric stove generates heat through conduction and convection. Also, equipment such as pumps and fans have frictional losses associated with them, which turn into additional heat supplied into the space. Thus, for the simulated electrical appliances, all the electrical power is turned into heat [86]. Details about the heat loads pertaining to different appliances are provided in Table 3.1 [3].

Table 3.1: Appliances Heat Fluxes [3]

Name	Oven	Fridge	TV	Lamp	Microwave	Waterpump	Inverter
Heat Load (W)	1318	100	110	3	800	90	260

In the reference case, the supply air is entering the domain with a uniform velocity 1.3 and direction of $(0, -1, 0)$ and constant temperature of 15°C [3]. As it is shown in Figure 3.2, the inlet grille for the AC system is located at the ceiling towards the back of the vehicle and the outlet is located close to the front seats. The turbulence intensity at inlet vent is 5.8% calculated by Eq. 3.2 [87]:

$$I = 0.16Re^{-\frac{1}{8}} \quad (3.2)$$

where I is the turbulence intensity and Re is the Reynolds number defined as:

$$Re = \frac{\rho u d_h}{\mu} \quad (3.3)$$

where d_h (m) is hydraulic diameter of the inlet, ρ (kg/m^3) is the density, μ (Ns/m^2) is the dynamic viscosity, and u (m/s) is the air velocity at the inlet. In the current study, the hydraulic diameter and the Reynolds number at the center of the inlet ventilation are $d_h = 0.36m$ and $Re = 3205$, respectively, based on the information provided by Erwin Hymer. The density is calculated using the ideal gas law. The outlet is defined as a zero static gauge pressure vent. As the computational analysis is limited to the interior space of the cabin, the radiative, conductive and convective heat transfer effects due to the interactions between the exterior environment and the interior compartment are modeled as constant heat fluxes through the boundaries. In the current study, same as [88] [89], the worst outdoor condition (i.e hottest conditions) is considered to evaluate the performance of AC system. The outdoor temperature is set to be $T_{outdoor} = 35^\circ C$, temperatures of all interior walls, and the floor are set $23^\circ C$, and heat fluxes are applied through exterior walls. The heat fluxes and the temperatures of the walls are summarized in Table 3.2 [88][89].

The radiative heat fluxes through the windows are considered as constants measured from [88]. The reason behind this decision is that the radiative heat flux depends on the position of the sun relative to the vehicle; hence, the heat flux would change due to the simulated time of day, the year, the weather, the location, surrounding buildings, etc. This means that to be able to compare the simulation results, similar conditions have to be assumed (i.e. constant radiative heat flux through windows). The combination of these cases represents the worst case scenario.

Table 3.2: Boundary condition settings for surfaces

Name	Temperature (°C)	Heat Flux ($\frac{W}{m^2}$)
Ceiling [88]	–	30
Floor [89]	23	–
Left Surface [88][89]	–	30
Right Surface [88][89]	–	30
Rear Surface [88][89]	–	30
Windshield [88][89]	–	385
Left Side Windows [88]	–	180
Right Side Windows [88]	–	180
Rear Windows [88]	–	180
Interior Surfaces [88][89]	23	–

3.1.3 Mesh Generation

To capture the viscous wall effects, the mesh near walls should be fine enough. By approaching the middle of the domain, the viscous effects are reduced, and high-resolution mesh is unnecessary. Therefore, an unstructured mesh with a Cartesian near mesh near the wall is used for these simulations. The boundary layer consists of 10 layers. In order to capture the most sensitive and critical locations with sufficient accuracy, fine mesh is applied to the edges and the surface of the vents, the appliances, and the windows. A focused view on some of the important features such as the vent, the side window, the water pump, and the inverter is shown in Figure 3.3.

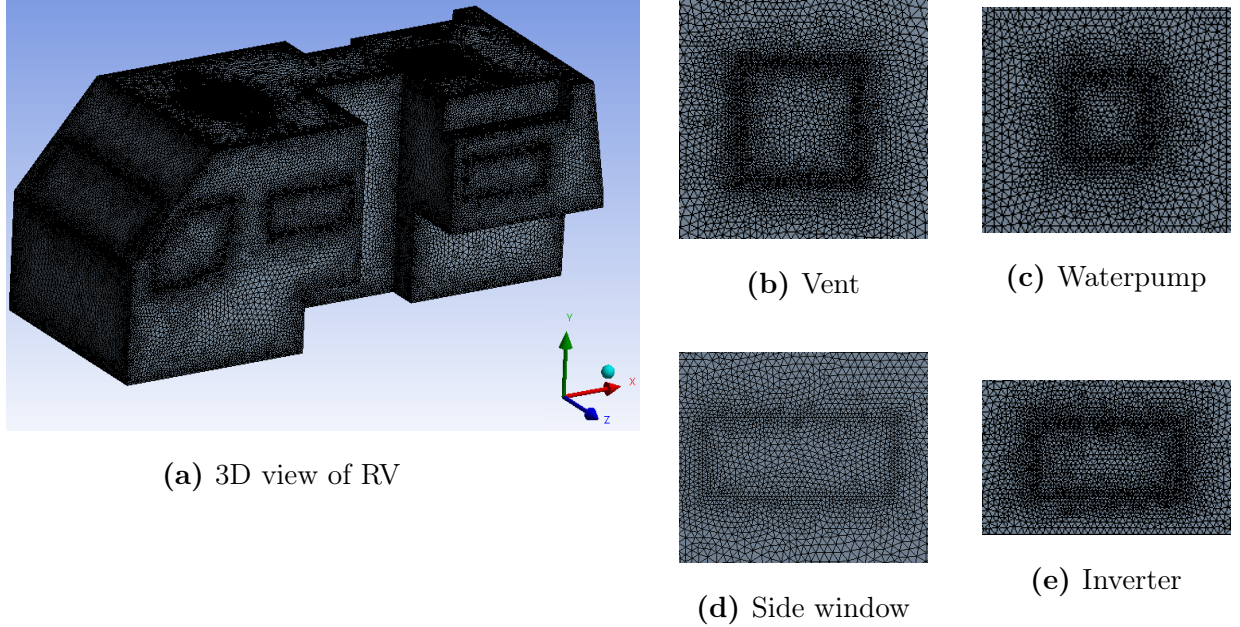


Figure 3.3: Focused view of important features.

The grid-independency analysis is implemented by considering three levels of mesh refinement. The summary of the different mesh size combinations is presented in Table 3.3. The average element length's size is decreasing from $0.0148m$ to $0.0099m$ to get a finer mesh. The thickness of the layer adjacent to walls in each mesh changes from $0.003m$ to $0.001m$, which imposes $y^+ < 5$ for all three cases. A line at the geometric center of the compartment from $(0, 1.0135, 0)$ to $(5.045, 1.0135, 0)$ in meters is defined. The comparison of temperature and velocity change on this line for the different meshes is presented in Figure 3.4 and 3.5. Mesh 2 and 3 show almost the same results; therefore, the second mesh, which has sufficient accuracy, is selected for continuing the analysis.

Table 3.3: Summary of the different mesh size combinations.

Features	Number of cells	Cell length (m)	First layer thickness (m)	y^+
Mesh 1	2,649,608	0.0148	0.003	4.5
Mesh 2	4,821,360	0.0126	0.002	2.95
Mesh 3	9,451,113	0.0099	0.001	1.48

The selected computational mesh has 4,821,360 tetrahedron cells (Figure 3.6). The maximum growth ratio is 1.05. The distance from the wall of the first cell center is 0.002 m. As a result, given the velocity at the boundaries, this mesh length leads to $y^+ = 1.48$.

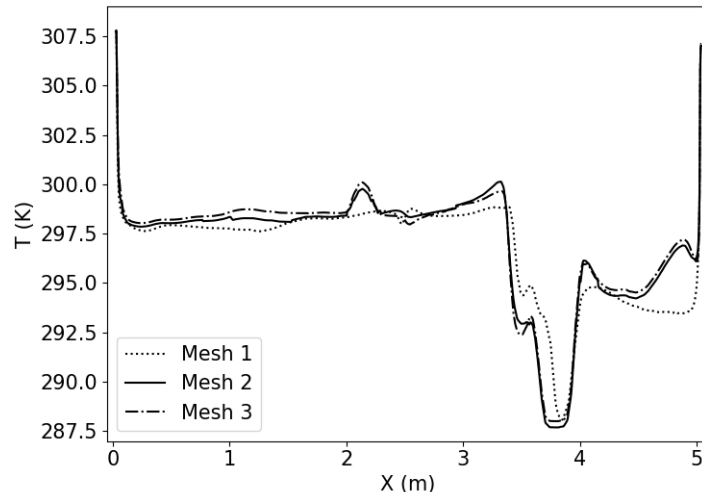


Figure 3.4: Mesh independency test (temperature change on the center-line of the cabin, from $(0, 1.0135, 0)$ to $(5.045, 1.0135, 0)$) at time $t=60s$.

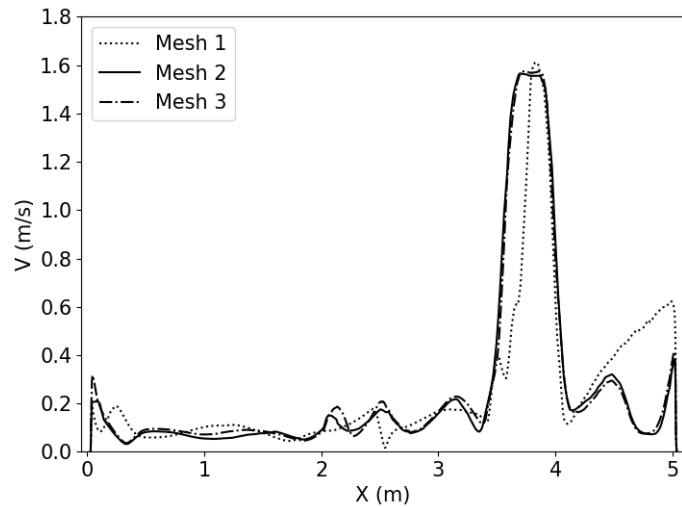


Figure 3.5: Mesh independency test (velocity change on the center-line of the cabin, from (0, 1.0135, 0) to (5.045, 1.0135, 0)) at time $t=60s$.

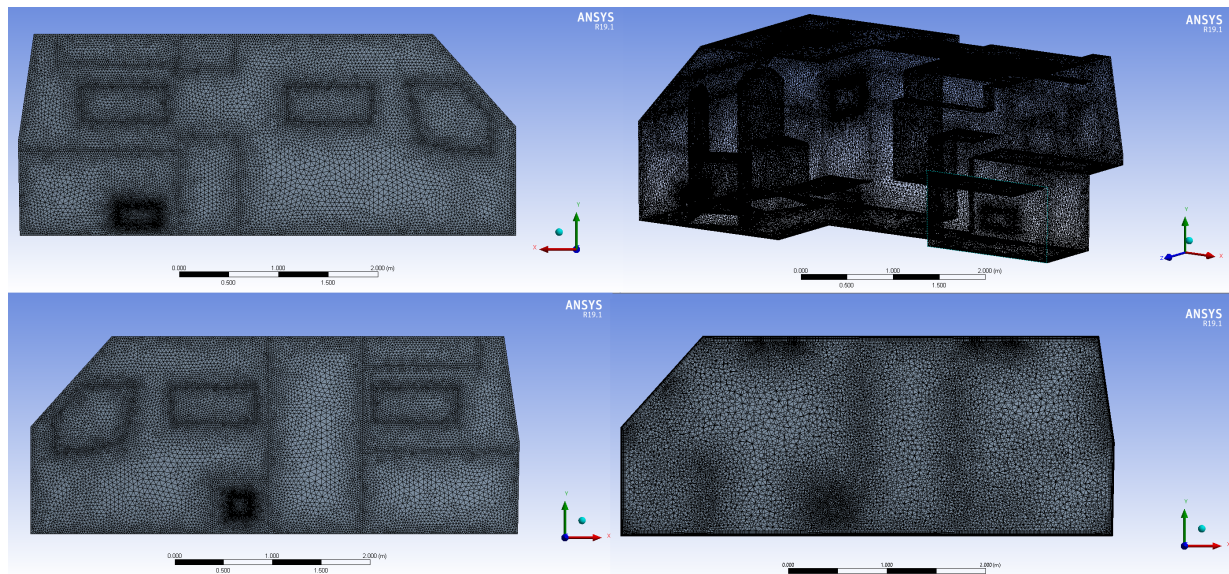


Figure 3.6: Selected computational mesh.

3.1.4 Selection of Turbulence Model and solver Setting

An appropriate turbulence model is needed for an accurate prediction of indoor airflow and in-cabin temperature distribution pattern. In the previous chapter, the reliability and adequacy of the RNG $k - \epsilon$ model for simulating air circulation and temperature distribution within a space is validated; hence, the RNG $k - \epsilon$ model is implemented for all simulations in the current study.

Transient 3D RANS equations are solved with a time step of $0.02s$ (for the sake of convergence of all cases and minimizing the computational costs) and a maximum of 20 iterations per time step. For pressure velocity coupling, the SIMPLE algorithm is applied. Also, for the convection, viscous, and pressure terms, second-order discretization schemes are implemented. The second-order implicit scheme is applied for the time integration.

3.1.5 Thermal Comfort Criteria

Thermal comfort is subjective and is not derived from the scientific principles; hence, it cannot be treated like the equations of heat and mass transfer or energy balance. The most popular technique for evaluating thermal comfort is PMV (Predicted Mean Vote), which categorizes thermal comfort level based on the average thermal sensation response of a large group of people (test subjects) by using the ASHRAE thermal sensation scale [4]. In the development of this scale, the test subjects' responses were studied while having various activity and clothing levels in environments with different air temperatures, humidity levels, air velocities, and airflow patterns. The ASHRAE thermal sensation scale is given in Table 3.4. Therefore, on the ASHRAE scale, the PMV index values are between -3 and 3. The closer the PMV value is to zero, the better the thermal comfort is within the space. The other practical index to predict the percentage of people with thermal dissatisfaction is

PPD (Predicted Percentage of Dissatisfied), which is dependent on the PMV value. This index is expressed in percentage.

Table 3.4: ASHRAE thermal sensation scale [4]

Sensation	PMV Value
Hot	+3
Warm	+2
Slightly Warm	+1
Neutral	0
Slightly Cool	-1
Cool	-2
Cold	-3

The PMV index value can be calculated from Eq 3.4:

$$\begin{aligned}
 PMV = & [0.303 \exp(-0.036M) + 0.028] \{ (M - W) - 3.05 \times 10^{-3} [5.733 - 6.99(M - W) \\
 & - p_a] - 0.42[(M - W) - 58.15] - 1.7 \times 10^{-5} M (5867 - p_a) - 0.0014 M (34 - t_a) \\
 & - 3.96 \times 10^{-8} f_{cl} [(t_{cl} + 273)^4 - (\bar{t}_r + 273)^4] - f_{cl} h_c (t_{cl} - t_a) \}
 \end{aligned} \tag{3.4}$$

where,

$$\begin{aligned}
 t_{cl} = & 35.7 - 0.028(M - W) - I_{cl} \{ 3.96 \times 10^{-8} f_{cl} [(t_{cl} + 273)^4 - (\bar{t}_r + 273)^4] \\
 & + f_{cl} h_c (t_{cl} - t_a) \}
 \end{aligned} \tag{3.5}$$

and,

$$h_c = \begin{cases} 2.38 |t_{cl} - t_a|^{0.25} & \text{for } 2.38 |t_{cl} - t_a|^{0.25} > 12.1 \sqrt{v_{ar}} \\ 12.1 \sqrt{v_{ar}} & \text{for } 2.38 |t_{cl} - t_a|^{0.25} < 12.1 \sqrt{v_{ar}} \end{cases} \tag{3.6}$$

$$f_{cl} = \begin{cases} 1.00 + 1.29l_{cl} & \text{for } l_{cl} \leq 0.078m^2 \text{ K/W} \\ 1.05 + 0.645l_{cl} & \text{for } l_{cl} > 0.078m^2 \text{ K/W} \end{cases} \quad (3.7)$$

where, W (W/m^2) is the effective mechanical power, h_C ($\frac{W}{m^2K}$) is the convective heat transfer coefficient, f_{cl} is the clothing surface area factor, p_a (Pa) is the vapour pressure of water, M ($\frac{W}{m^2}$) is the metabolic rate, l_{cl} ($\frac{m^2.K}{W}$) is the clothing insulation, t_{cl} ($^\circ C$) is the clothing surface temperature, t_a ($^\circ C$) is the air temperature, v_{ar} ($\frac{m}{s}$) is the relative air velocity and \bar{t}_r ($^\circ C$) is the mean radiant temperature.

The PPD index is calculated by the following equation:

$$PPD = 100 - 95 \exp [-(0.03353PMV^4 + 0.2179PMV^2)] \quad (3.8)$$

In the current study, constant metabolic rate $M = 1Met$, constant clothing insulation resistance $l_{cl} = 1 clo$, and constant relative humidity $RH = 50\%$ are assumed for the calculation of PMV. These numbers are based on the existing literature in order to provide the means to compare the results from this study to other researchers' works [30][89]. It should be noted that $1 clo = 0.155 \frac{m^2 \circ C}{W}$ and $1 Met = 58.2 \frac{W}{m^2}$.

For calculation of PMV and PPD indices, a Python code is written, which is able to calculate these indices based on given values for clothing insulation, temperature, metabolic rate, humidity ratio, and velocity parameters. The temperature and velocities are extracted from ANSYS Fluent at all points of interest. The code is presented in Appendix A.

Beside evaluating thermal comfort by the PMV index, it is also possible to gauge the thermal comfort using the temperature. The bounds for these variables are adapted from ASHRAE 55 [4]. The range of acceptable temperatures according to this standard is between 20 and $25.6^\circ C$.

3.1.6 Model Development

It is important to note that the calculations in this study are based on the worst-case scenario (maximum internal temperature and heat generation). This means that the calculated total heat flux corresponds to all appliances running simultaneously, along the hottest ambient conditions in order to simulate the hottest conditions within the RV's cockpit. Moreover, the following conditions are considered in the simulations:

1. The RV is in stationary mode, with its engine turned off.
2. The temperature, PMV, and PPD profiles are investigated along three lines. The reason is that achieving thermal comfort in the entire domain is costly and unnecessary (for example in the regions close to the ceiling or the corners). Therefore, instead of having a global metric for assessing thermal comfort, the PMV and PPD values are investigated in locations where the occupants spend most of their time in the RV. It should be noted that these three lines are good representations of the thermal comfort within the vehicle's most important locations. These lines are located near the driver seat (line1), middle of the cabin (line2), and near the bed (line3). Table 3.5 lists the coordinates for these lines. These lines are considered from 0.7m to 1.7m, which is a representation of the breathing zone in the cabin. The breathing zone is defined as “the region within an occupied space between 3 and 6 feet above the floor and more than 2 feet from walls or fixed air-conditioning equipment” [4].

Table 3.5: Coordinates of allocated measuring lines.

Location	Coordinates					
	<i>X</i> ₁	<i>Y</i> ₁	<i>Z</i> ₁	<i>X</i> ₂	<i>Y</i> ₂	<i>Z</i> ₂
Line 1 (Driver Seat)	0.86	0.7	0.6	0.86	1.7	0.6
Line 2 (Middle Area)	2.4	0.7	-0.2	2.4	1.7	-0.2
Line 3 (Bed)	4.5	0.7	0	4.5	1.7	0

3. All simulations have a total runtime of 200 seconds. This duration is selected in a way that the simulation of the reference case reaches a steady-state within this time. Another constraint that led to this decision is the time it takes to run each simulation. For example, 200 seconds simulation runtime for this study takes almost three days, which is very computationally expensive. Each simulation is done by the use of two nodes, each containing 32 CPUs. In addition, the goal is that temperature at all these three locations of interest reaches the desired temperature range (21 °C to 25 °C). If the results from any of the simulations show that the temperature does not reach this desired range within 200 seconds, it implies that those simulated cases consume much more energy than the reference case to achieve the same outcome; hence, further investigations with longer duration have not pursued those cases.
4. There is no passenger in the cabin.
5. The cabin door and windows are closed.

Parametric Study

Six different cases are modeled for evaluating the levels of thermal comfort in the cabin. The current study is done parametrically, where the impact of changing various parameters is evaluated using CFD. The following four parameters are the focus of this parametric study:

1. Direction of supply airflow
2. Location of the AC inlet
3. Location of the exhaust vent
4. Number of the exhaust vent

These parameters will be explained further for each simulation case. In this study, the AC system is installed on the roof of the RV, and consequently, the inlet vents are placed along the ceiling. To decrease the effect of recirculation zones created close to the ceiling, the outlet vents are located at the ceiling as well. Additionally, considering the constraint caused by the interior design of RV and in order to have sufficient fluid flow, the vents should be placed almost at the x-centerline of the ceiling.

3.2 Results and Discussion

In this section, seven different cases of the parametric study will be investigated. For this purpose, temperature and velocity magnitude contours are evaluated on different planes within the cabin. Also, the temperature, PMV, and PPD values changes along the y coordinate at the designated lines are presented for each case.

3.2.1 Reference Case

In the first scenario, the reference case is modeled based on the existing assumptions. All other cases are compared with this case. In the reference case, the inlet air temperature and velocity are set to 16°C and $1.3 \frac{\text{m}}{\text{s}}$, respectively. Under the worst surrounding conditions, the ambient air temperature is 35°C , and the solar heat flux absorbed by the RV's windows are substituted from experimental measurements conducted at the same surrounding condition [88]. Table 3.6 shows a summary of the reference case's boundary conditions.

The velocity magnitude and the temperature contours at different sections are shown in Figure 3.7 and 3.8. As shown in these figures, the supplied air impinges on the floor and then redirects to sides. The entrained stationary air beside the supplied air leads to a larger cold zone near the impinging zone. Due to the high momentum of this region, the cold air is distributed effectively through the cabin. It is expected that by increasing the entrainment, better cold-air mixing takes place. For this purpose, the impinging cold-air should keep its high momentum near the floor.

Two heat transfer mechanism is considered between the walls and air within the cabin, namely conduction, and convection. It is estimated that the dominant heat transfer mechanism at regions with higher velocity is convection, while, at the region with low velocity, the dominant mechanism is conduction. Near the floor, high velocity leads to higher convection, and the temperature of the flow decreases effectively in the middle of the floor. Due to the configuration of inlets and outlet vents, a low-velocity region (circulation zone) is created in the middle of the ceiling. At this location, the heat flux is transferred from the wall to the air by conduction mechanism, and circulation brings about a hot zone.

The corresponding temperature, PMV, and PPD values at the designated lines are shown in Figure 3.9, 3.10, and 3.11, respectively. In addition, spatially-averaged temper-

Table 3.6: Boundary conditions used in the reference case.

Inlet velocity ($\frac{m}{s}$)	Inlet air temperature ($^{\circ}\text{C}$)	Velocity vector (Normal to inlet surface)	Center of inlet vent			Center of exhaust vent		
			X (m)	Y(m)	Z(m)	X(m)	Y(m)	Z(m)
1.3	16	(0, -1, 0) (Normal to inlet surface)	4.383	2.024	0	1.569	2.024	0

ature versus time is plotted in Figure 3.12 for the reference case. This plot clearly shows that after 200 second, the solution reaches a steady state. In Figure 3.13, temperature contour at 240 seconds and 200 seconds are compared, which reveals that spatial temperature changes after 200 seconds are negligible.

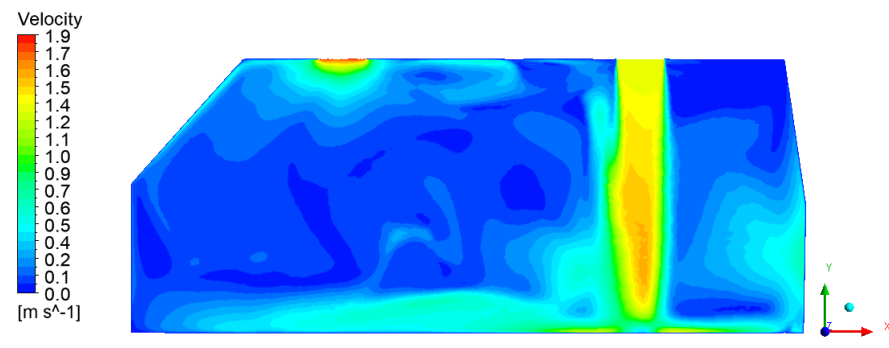
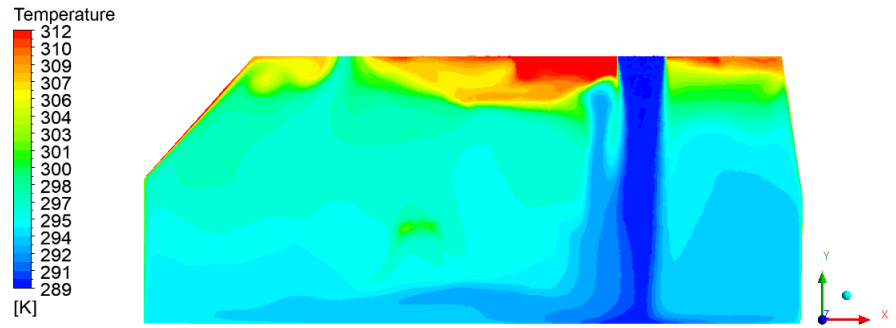
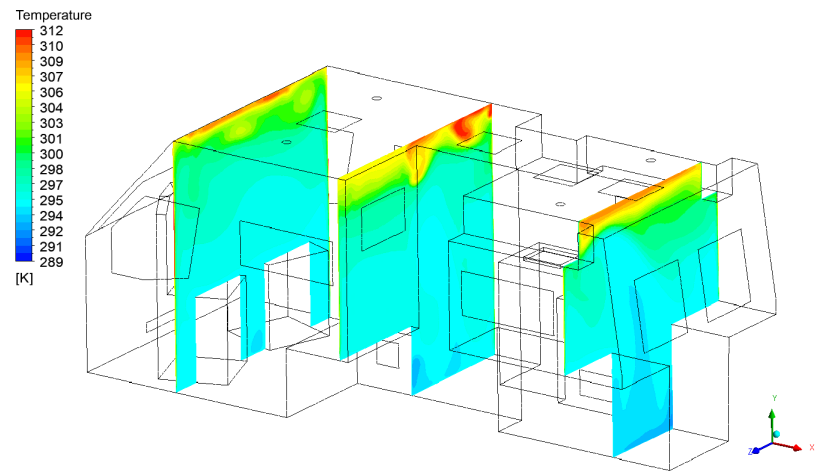
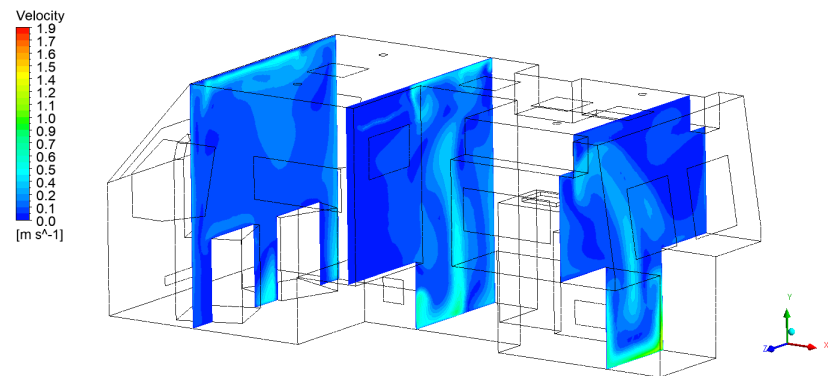


Figure 3.7: Contours of reference case at $t = 200s$: (a) temperature distribution and (b) velocity magnitude at $Z = 0$ (XY Plane).



(a)



(b)

Figure 3.8: Contours of reference case at $t = 200s$: (a) temperature distribution and (b) velocity magnitude at $X = 0.86m$, $X = 2.4m$, and $X = 4.5m$ (YZ Planes)

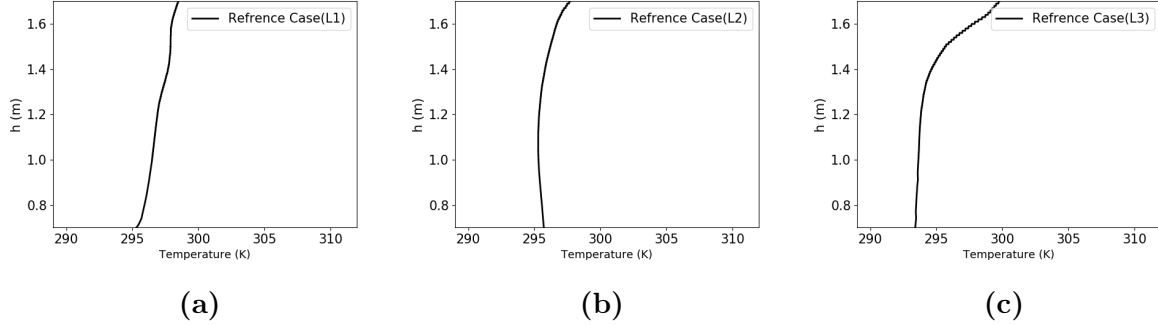


Figure 3.9: Temperature profiles at $t = 200s$ along (a)line 1, (b)line 2, and (c)line 3.

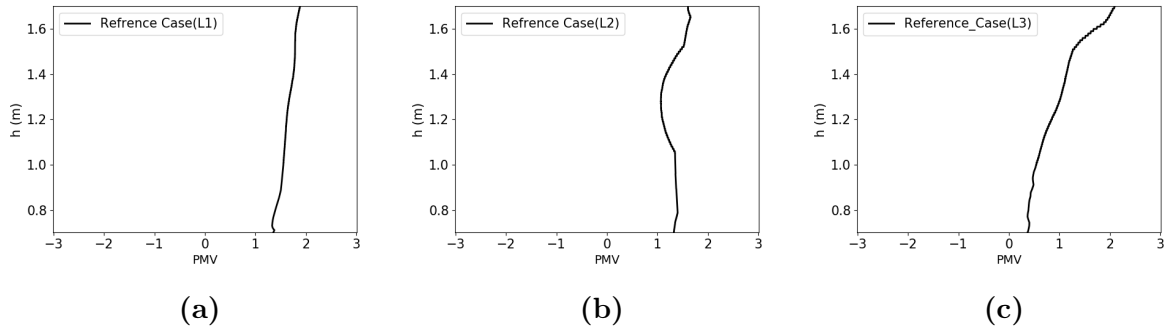


Figure 3.10: PMV profiles at $t = 200s$ along vertical lines at (a)line 1, (b)line 2, and (c)line 3.

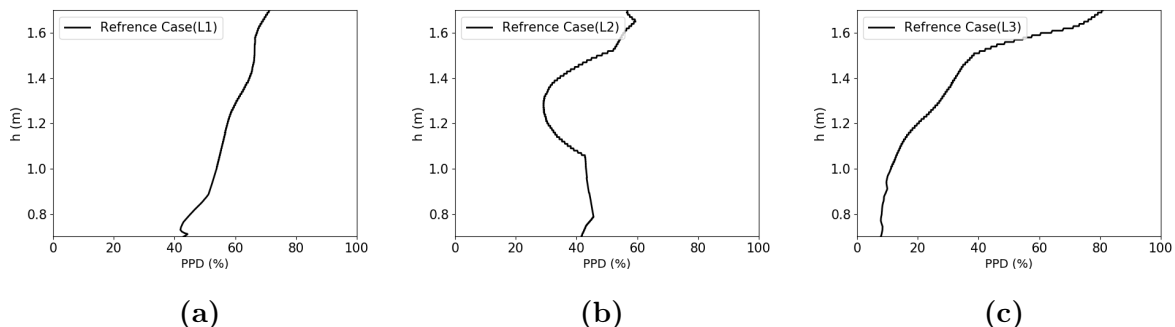


Figure 3.11: PPD profiles at $t = 200\text{s}$ along vertical lines at (a)line 1, (b)line 2, and (c)line 3.

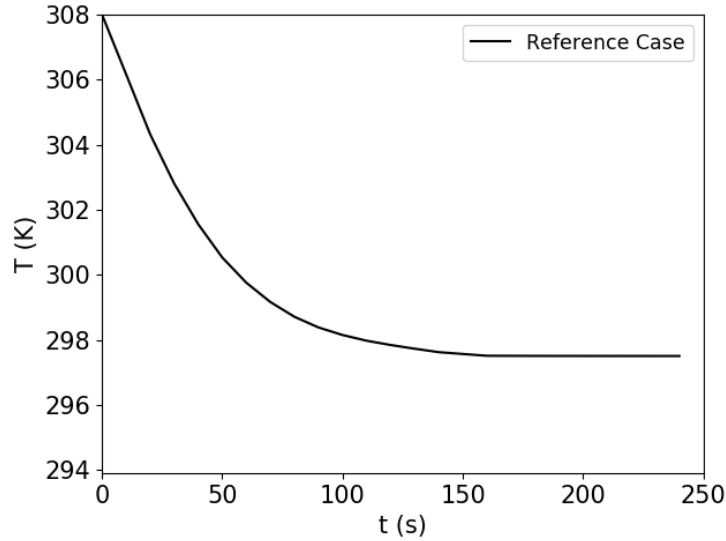


Figure 3.12: Transient simulation of spatially-averaged temperature for reference case.

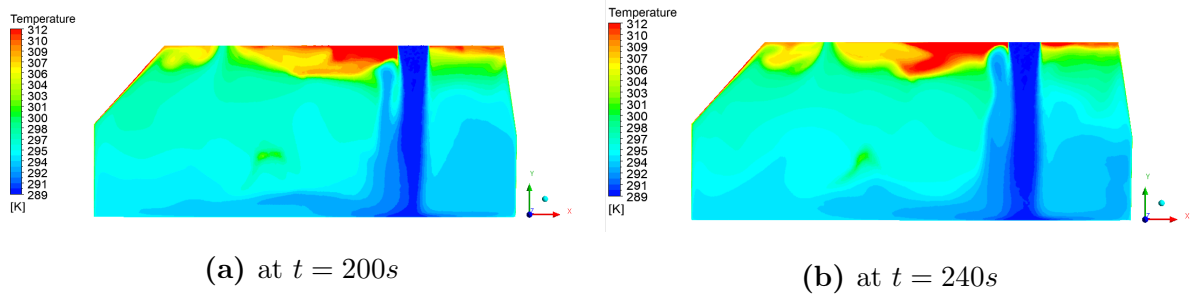


Figure 3.13: Temperature distribution at $Z = 0 \text{ m}$ for reference case.

3.2.2 RV compartment with and without AC system

A comparison between the interior temperatures and velocity magnitude in the RV compartment, with and without an AC system, are shown in Figure 3.15, 3.16, and 3.17. In both cases, heat gain by the air inside the cabin is attributed to the simultaneous operation

of all the appliances as well as the ambient environment's effects after 100 seconds. The temperature increase in the compartment without AC is significant. Also, as expected, the case without AC approximately has zero velocity all around the space. Figure 3.14 compares the temperature along y-axis at designated lines. Comparing the temperature inside the cabin of both cases in this figure shows how effective the AC is in cooling the space. For example, the temperature in the case with AC running at line 2 is between 22 °C and 25 °C, while in the case with the AC turned off, the temperature at the same line is between 33 °C and 39 °C. In total, the average temperature inside the cabin with and without AC system running is 298.15°C and 308.78°C, respectively, which indicates 10 °C temperature difference between these two conditions.

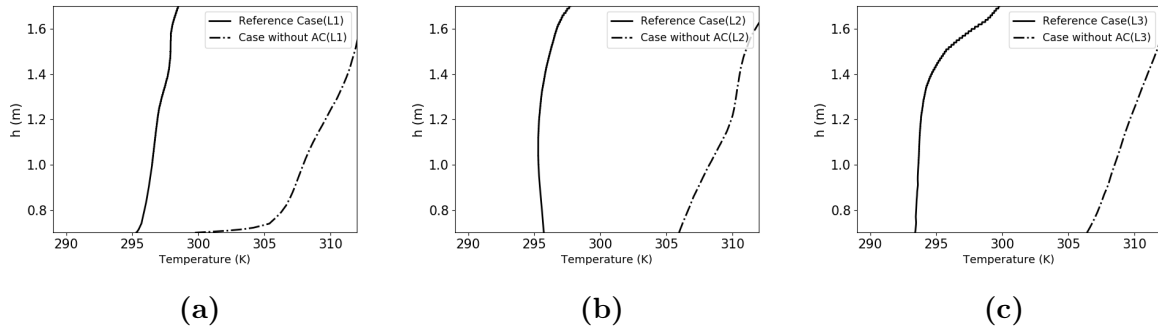


Figure 3.14: Temperature profiles at $t = 200s$ along (a) line 1, (b) line 2, and (c) line 3.

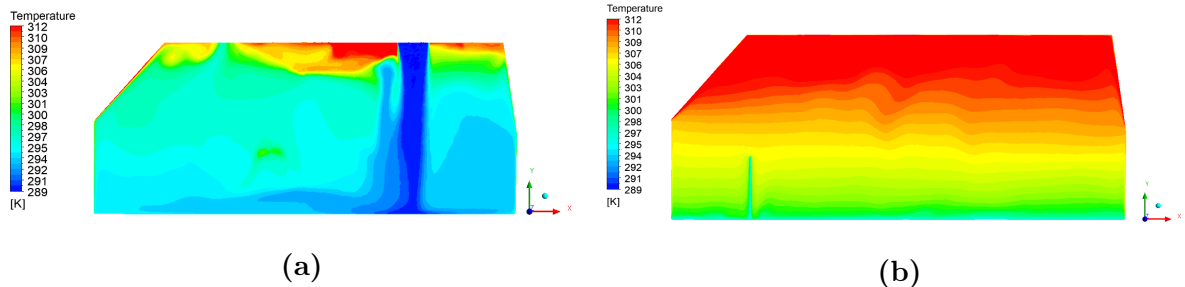


Figure 3.15: Temperature distribution at $Z = 0m$ (a) reference case (b) case without AC ($t = 200s$).

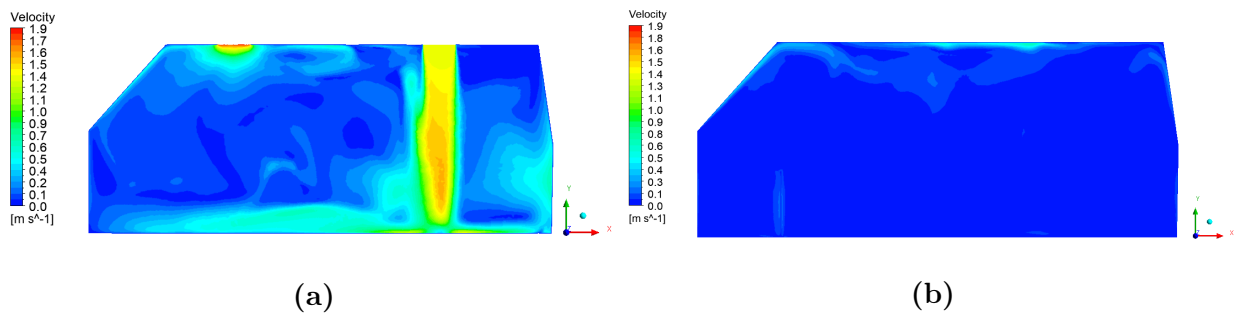


Figure 3.16: Velocity magnitude at $Z = 0m$ (a) reference case (b) case without AC ($t = 200s$).

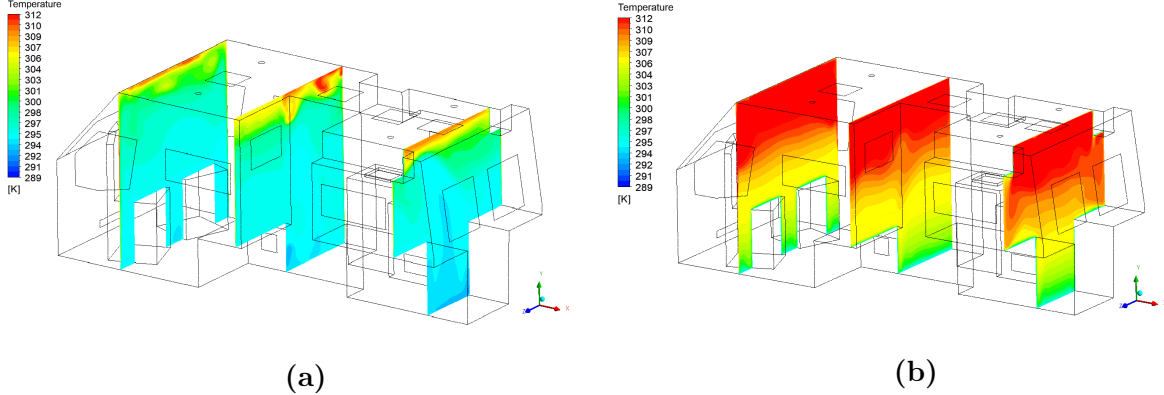


Figure 3.17: Temperature distribution at $X = 0.86m$, $X = 2.4m$, and $X = 4.5m$ (a) reference case (b) case without AC ($t = 200s$).

3.2.3 Impact of the Direction of Supply Air Flow

In order to study the impact of the direction of supply air flow, two simulations are set up with various velocity vectors. Previously, in the reference case, the air was supplied vertically. In order to change the inlet air angle, the x, y, z coordinates for the vent velocity vectors are modified from $(0, -1, 0)$ to $(-0.866, -0.5, 0)$ and $(0.866, -0.5, 0)$. The inlet velocity vector is always parallel to the XY plane. A schematic diagram of these modified velocity vectors are shown in Figure 3.18. In this figure, theta represents the angle between the velocity vector and the positive x axis on the ceiling.

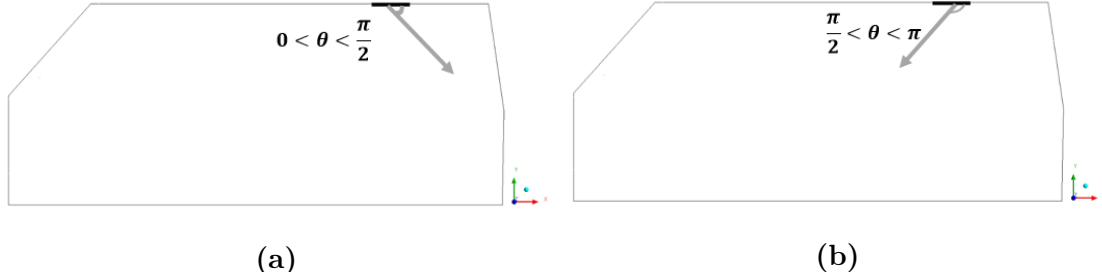


Figure 3.18: Schematic of velocity vectors.

The temperature and velocity magnitude contours for these cases are shown in Figure 3.41, 3.42, 3.43, and 3.44. Moreover, a comparison of temperature, PMV, and PPD values along Y-axis at the designated lines are presented in Figure 3.45, 3.46, and 3.47, respectively. These figures demonstrate a dramatic change in the airflow pattern caused by modification of the angle of the inlet velocity vector. As shown, angle modification leads to an inefficient mixing of the fresh air and undesirable temperature distribution within the cabin. In case 1, there is a low level of entrainment before impinging, and a small cold region is created, which causes inefficient cooling. On the other hand, although case 2 has a high level of entrainment, the momentum at the impinging region is not high enough, which results in inefficient air mixing. Consequently, the reference case provides a more desirable condition for temperature distribution.

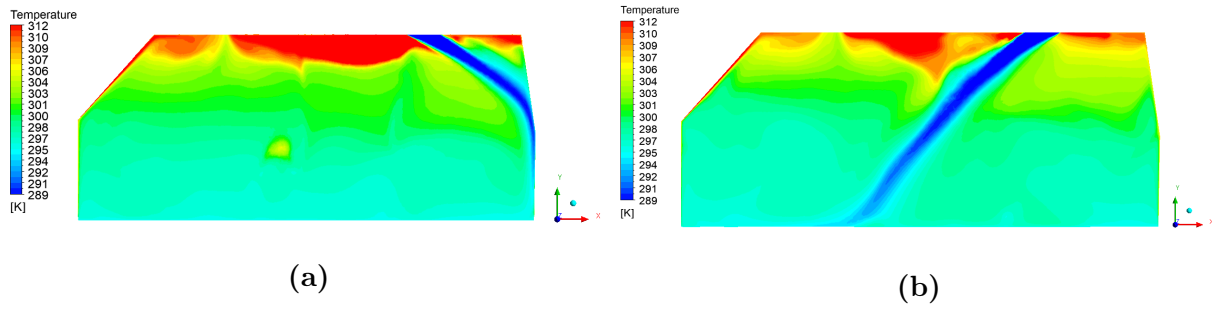


Figure 3.19: Temperature distribution at $Z = 0m$ for (a) case 1 (b) case 2 ($t = 200s$).

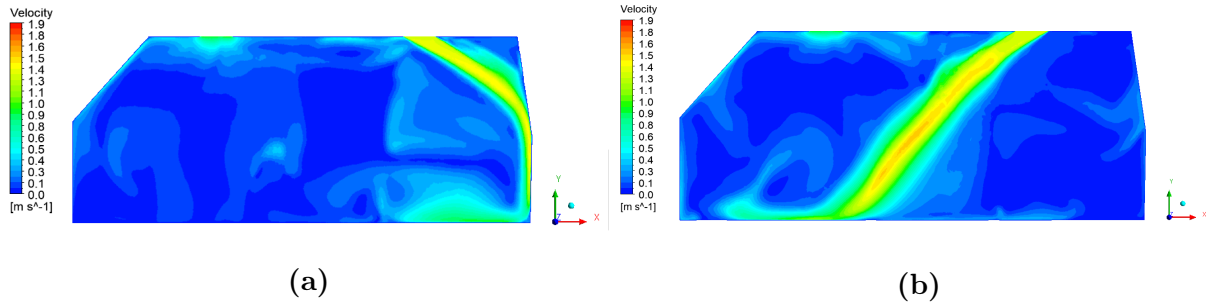


Figure 3.20: Velocity magnitude at $Z = 0m$ for (a) case 1 (b) case 2 ($t = 200s$).

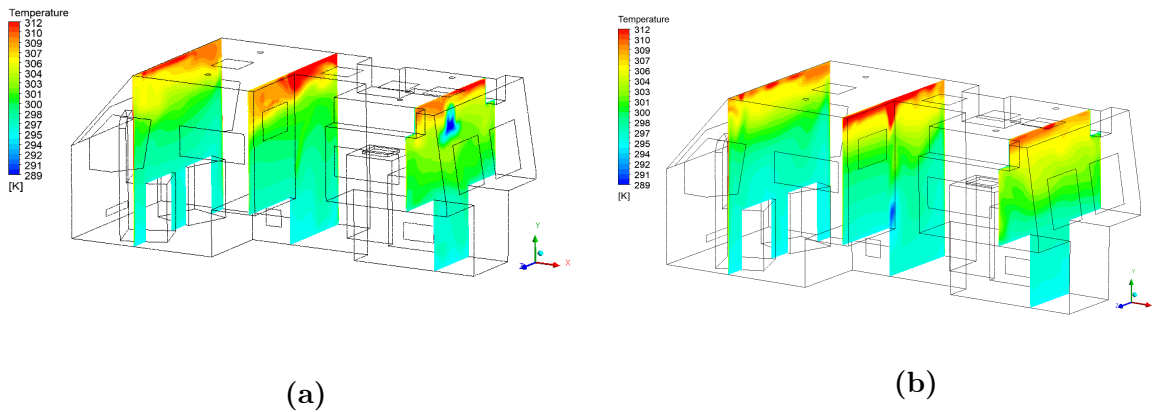


Figure 3.21: Temperature distribution at $X = 0.86m$, $X = 2.4m$, $X = 4.5m$ for (a) case 1 (b) case 2 ($t = 200s$).

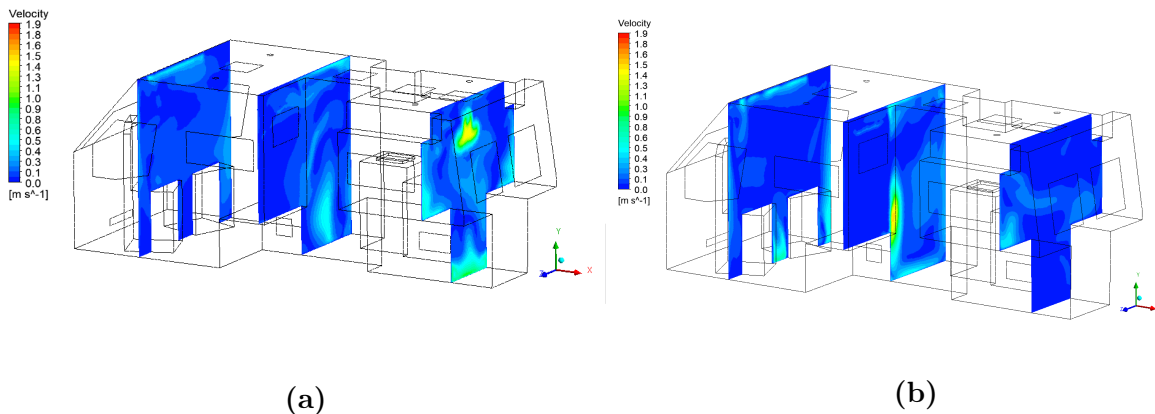


Figure 3.22: Velocity magnitude at $X = 0.86m$, $X = 2.4m$, $X = 4.5m$ for (a) case 1 (b) case 2 ($t = 200s$).

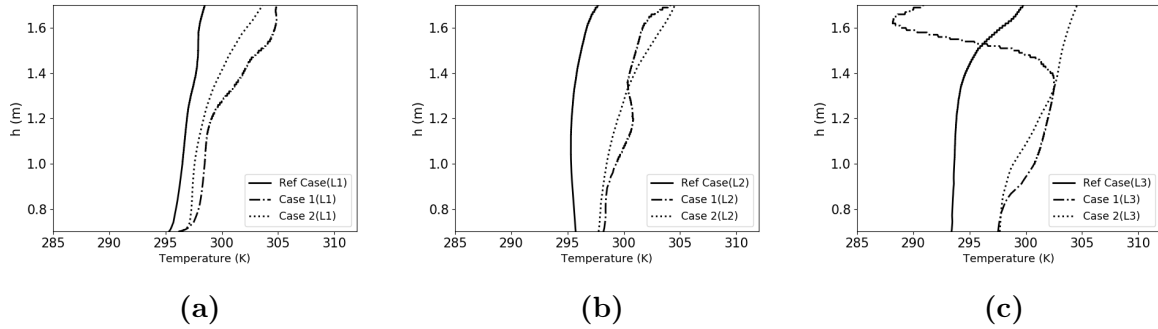


Figure 3.23: Temperature profiles for case 1, case 2, and reference case along (a) line 1, (b) line 2, and (c) line 3 ($t = 200s$).

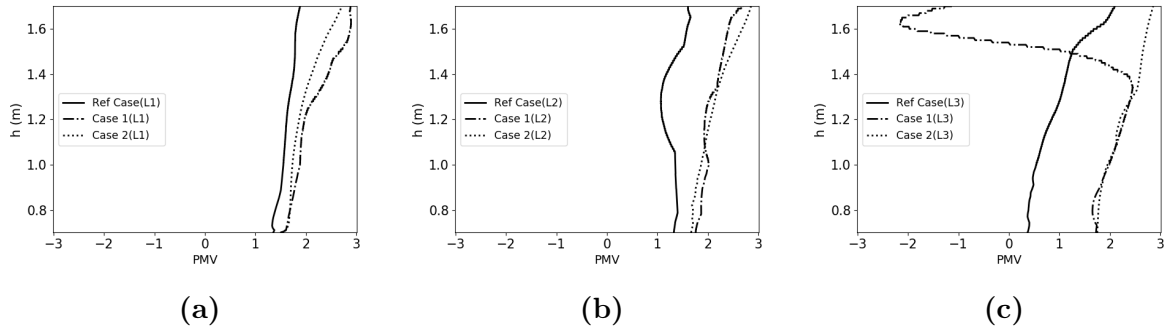


Figure 3.24: PMV profiles for case 1, case 2, and reference case along (a) line 1, (b) line 2, and (c) line 3 ($t = 200s$).

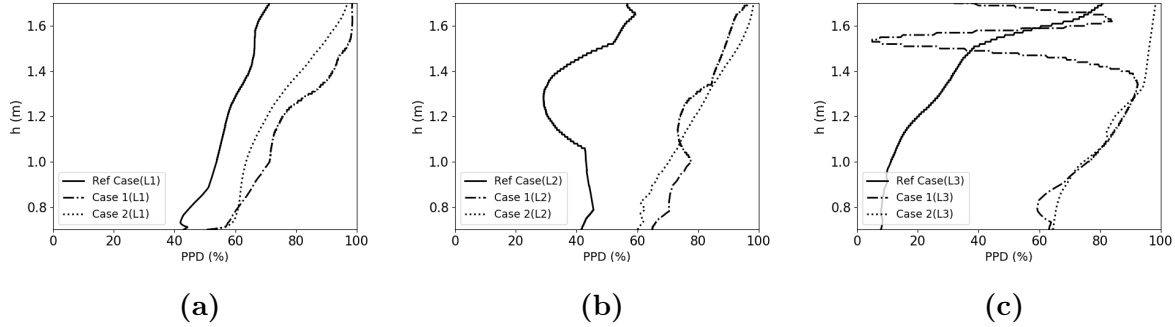


Figure 3.25: PPD profiles for case 1, case 2, and reference case along (a) line 1, (b) line 2, and (c) line 3 ($t = 200s$).

3.2.4 Impact of the location of AC Inlet

Two more cases are studied with different inlet locations than the reference case, while all other parameters are kept constant. Figure 3.26 shows the approximated vents' locations on the ceiling. The exact position of the vents are listed in Table 3.7. The inlet and outlet dimensions in case 3, case 4, and the reference case are all 0.36×0.36 .

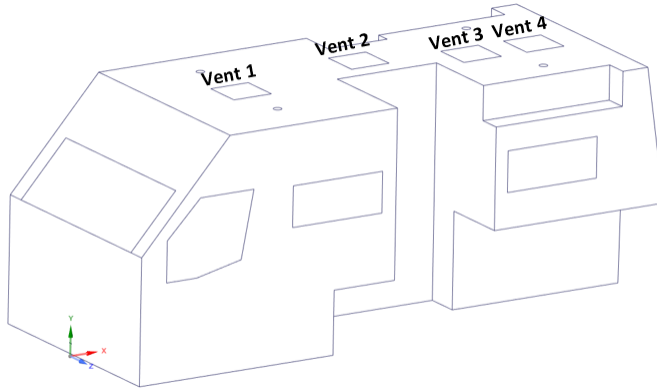


Figure 3.26: Vent locations.

Table 3.7: Vent coordinates for cases 3, 4 and the reference case.

Scenario	Inlet	Outlet	Center of inlet			Center of outlet		
	location	location	X(m)	Y(m)	Z(m)	X(m)	Y(m)	Z(m)
Reference Case	vent 3	vent 1	3.78	2.027	0	1.57	2.027	0
Case 3	vent 2	vent1	2.9	2.027	0.28	1.57	2.027	0
Case 4	vent 4	vent 1	3.78	2.027	0	1.57	2.027	0

Figure 3.27, 3.28, 3.29, and 3.30 present the temperature distribution and velocity magnitude for case 3 and case 4. Temperature profiles, PMV, and PPD values along Y-coordinates at line1, line2, and line 3 are compared in Figure 3.31, 3.32, and 3.33, respectively. It can be seen from these figures how the AC inlet location affects the temperature distribution inside the cabin. When vent 2 is selected as the inlet panel location, the region close to the driver tends to be colder compared to the reference case and the rear region of the RV tends to be hotter. Moreover, hot zones are smaller when the inlet is located at vent 2. The disadvantage of choosing the center of the RV for the location of inlet vent is that the supplied air would be short-circuited, meaning that most of the fresh air is exhausted before being circulated around the space and the air in the rear parts of cabin (close to the line 3) has higher temperature relative to the other two cases.

By choosing vent 4 as the inlet location, the distance between the inlet and outlet vent is increased, and the air spends more time inside the cabin. The recirculation zone near the ceiling enlarges, and the entrainment on the right side of the inlet vent is not beneficial for cooling the entire cabin space. This situation results in inefficient air circulation. Accordingly, case 4 does not provide desirable temperature; however, case 3 and the reference case show almost identical behavior with more advantages effective fresh air circulation.

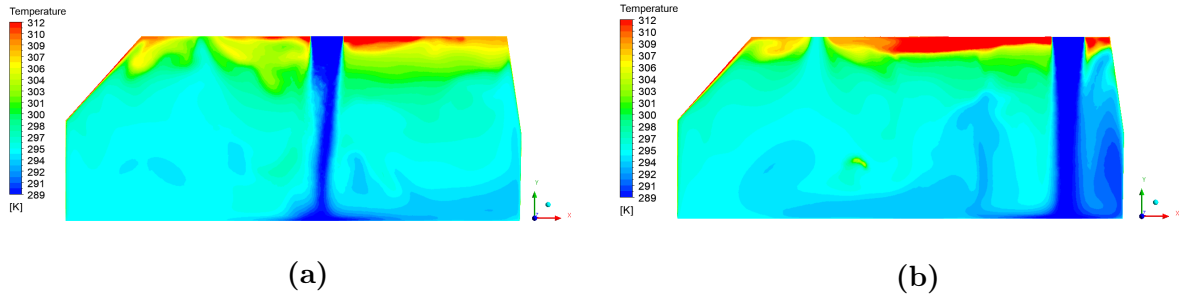


Figure 3.27: Temperature distribution at $Z = 0m$ for (a) case 3 and (b) case 4 ($t = 200s$).

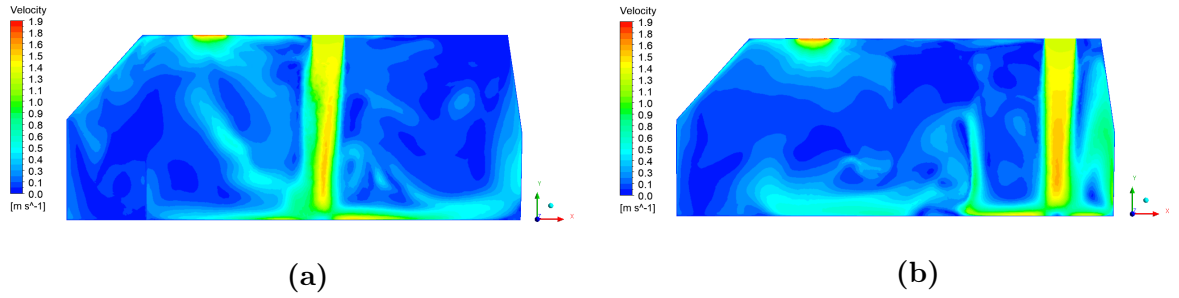


Figure 3.28: Velocity magnitude at $Z = 0m$ for (a) case 3 (b) case 4 ($t = 200s$).

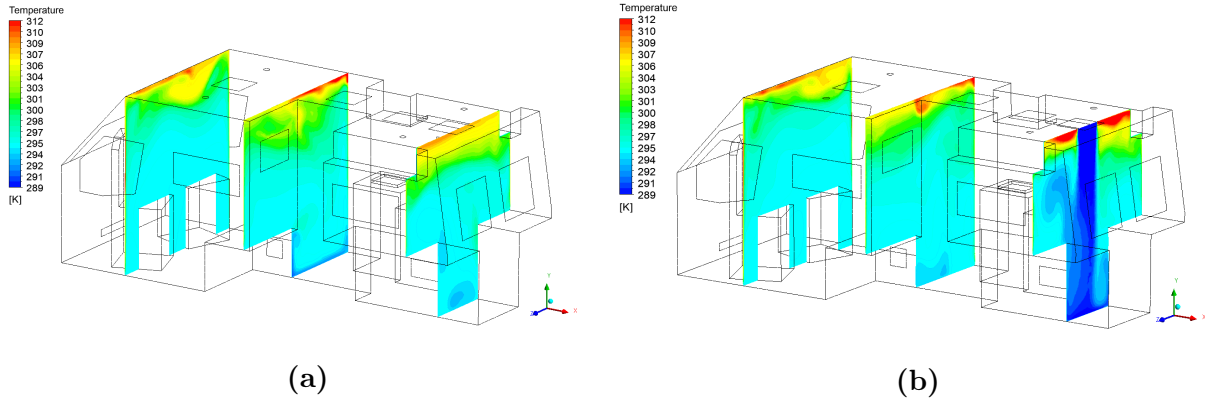


Figure 3.29: Temperature distribution at $X = 0.86m$, $X = 2.4m$, $X = 4.5m$ for (a) case 3 (b) case 4 ($t = 200s$).

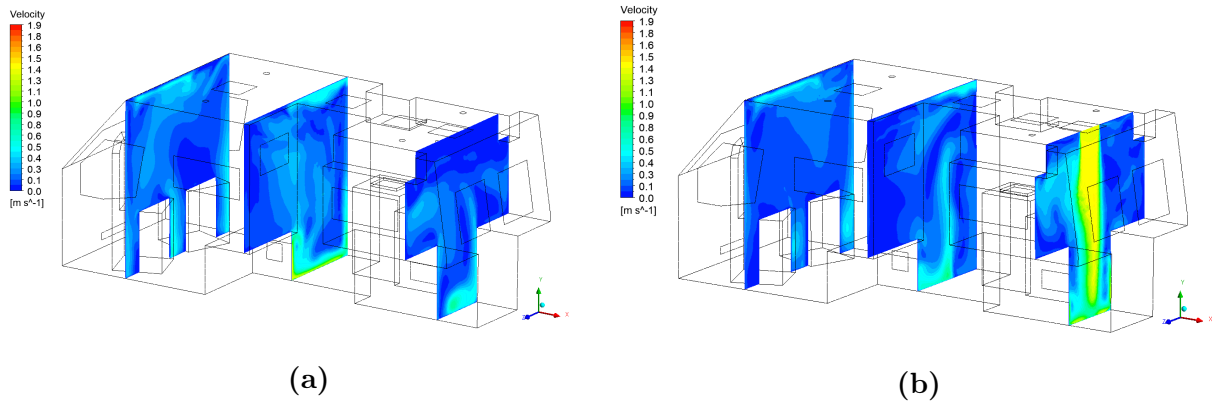


Figure 3.30: Velocity magnitude at $X = 0.86m$, $X = 2.4m$, $X = 4.5m$ for (a) case 3 (b) case 4 ($t = 200s$).

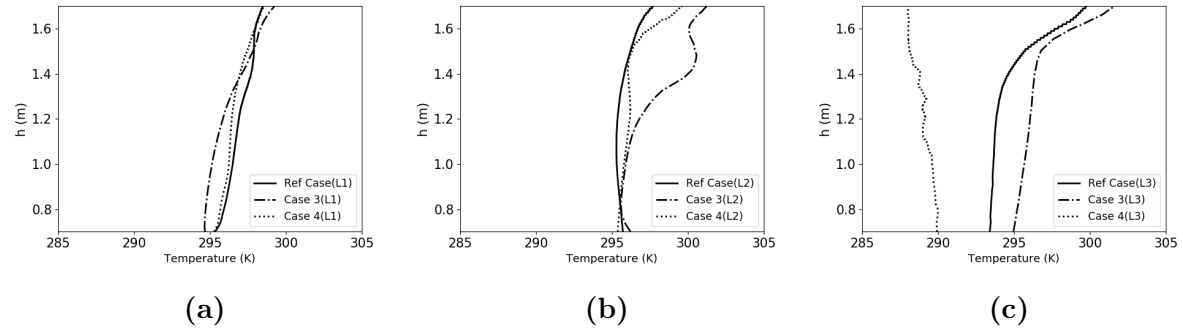


Figure 3.31: Temperature profiles for case 3, case 4, and reference case along (a) line 1, (b) line 2, and (c) line 3 ($t = 200s$).

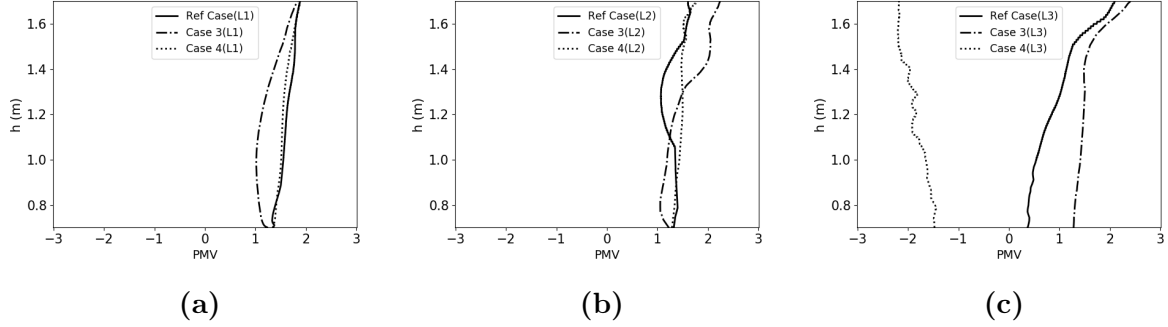


Figure 3.32: PMV profiles for case 3, case 4, and reference case along (a) line 1, (b) line 2, and (c) line 3 ($t = 200s$).

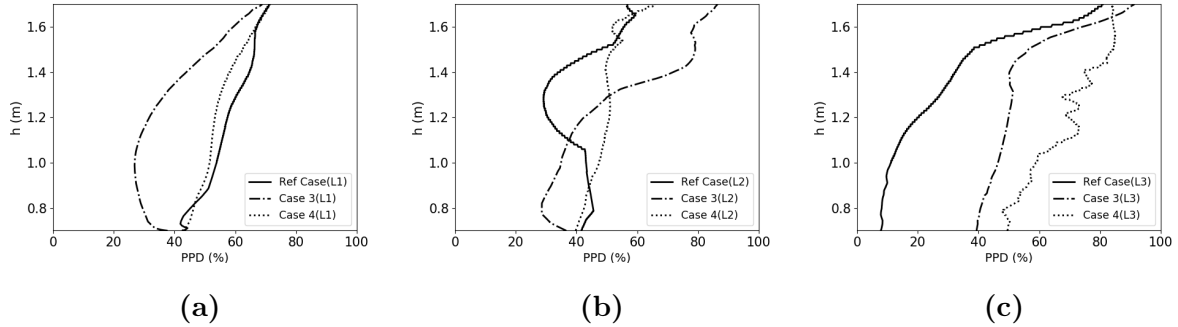


Figure 3.33: PPD profiles for case 3, case 4, and reference case along (a) line 1, (b) line 2, and (c) line 3 ($t = 200s$).

3.2.5 The Impact of Outlet Location

Similar to the previous section, all other parameters are kept constant but the outlet location. A new case is simulated with different outlet vent location. This location is approximately shown in Figure 3.26 and more details are listed in Table 3.8.

Table 3.8: Vent coordinates for case 5 and the reference case.

Scenario	Inlet	Outlet	Center of inlet			Center of outlet		
	location	location	X(m)	Y(m)	Z(m)	X(m)	Y(m)	Z(m)
Reference Case	vent 3	vent 1	3.78	2.027	0	1.57	2.027	0
Case 5	vent 3	vent 4	3.78	2.027	0	4.38	2.027	0

Contours of temperature and velocity magnitude of this case are compared with the reference case in Figure 3.34, 3.35, 3.36, and 3.37. As can be seen, case 5 leads to better air circulation and, accordingly, a more desirable temperature distribution at the rear part of the compartment. These results are more obvious in the temperature, PMV, and PPD diagrams at line 3 shown in Figure 3.38, 3.39, and 3.40. At line 1 and line 2 locations, the reference case shows better conditions of the temperature field.

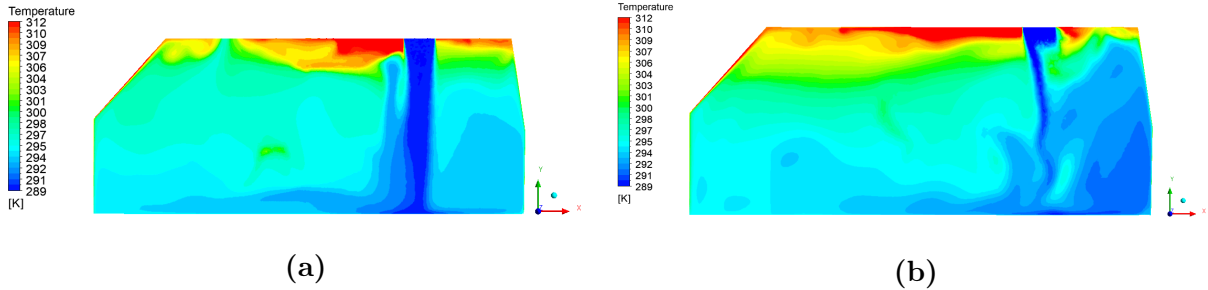


Figure 3.34: Temperature distribution at $Z = 0m$ for (a) reference case (b) case 5 ($t = 200s$).

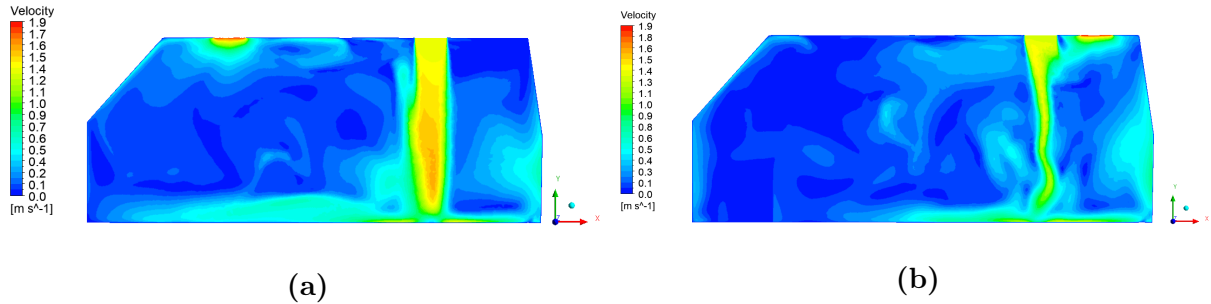


Figure 3.35: Velocity magnitude at $Z = 0m$ for (a) reference case (b) case 5 ($t = 200s$).

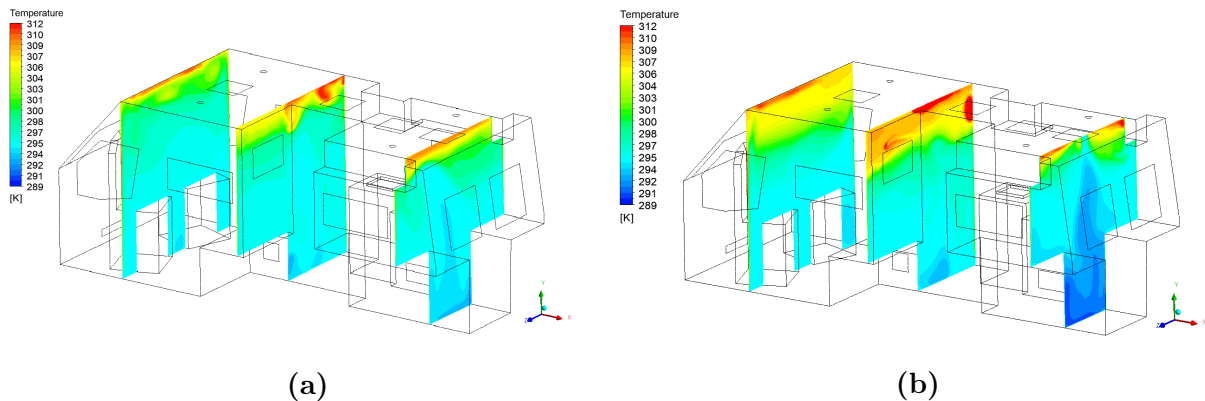


Figure 3.36: Temperature distribution at $X = 0.86m$, $X = 2.4m$, $X = 4.5m$ for (a) reference case (b) case 5 ($t = 200s$).

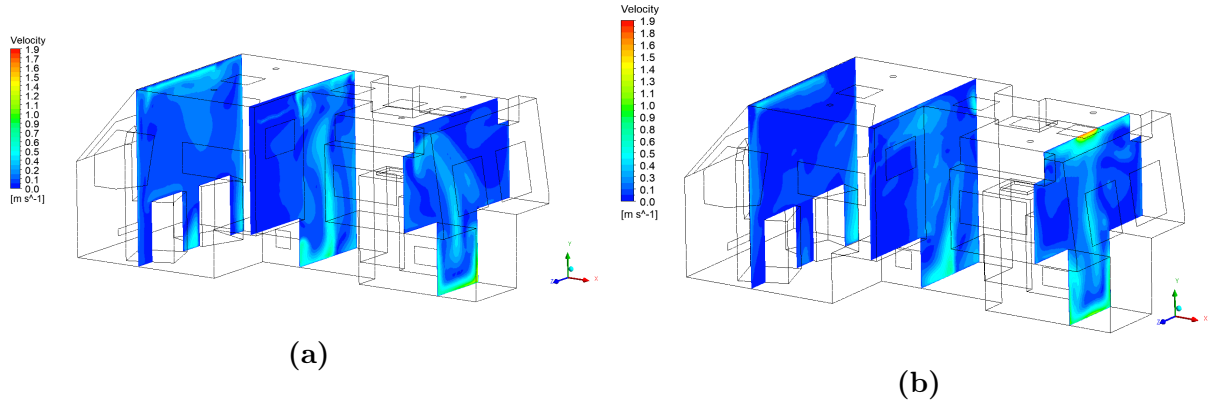


Figure 3.37: Velocity magnitude at $x=0.86\text{m}$, $x=2.4\text{m}$, $x=4.5\text{m}$ for (a) reference case (b) case 5 ($t = 200\text{s}$).

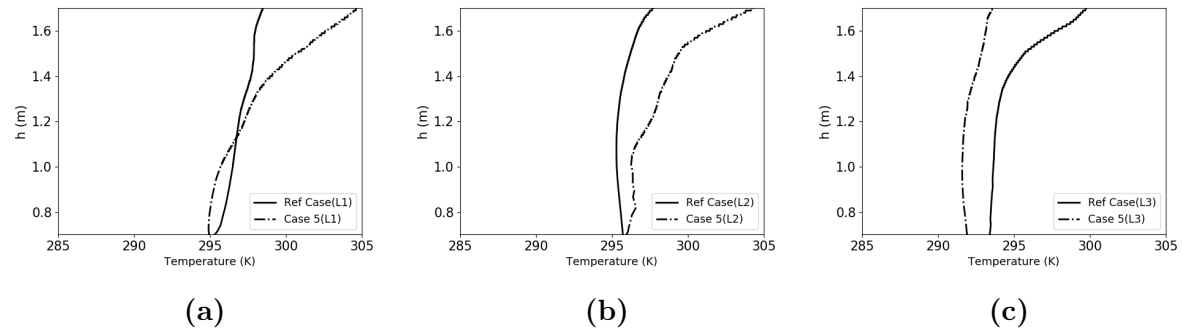


Figure 3.38: Temperature profiles for case 5 and reference case along (a) line 1, (b) line 2, and (c) line 3 ($t = 200\text{s}$).

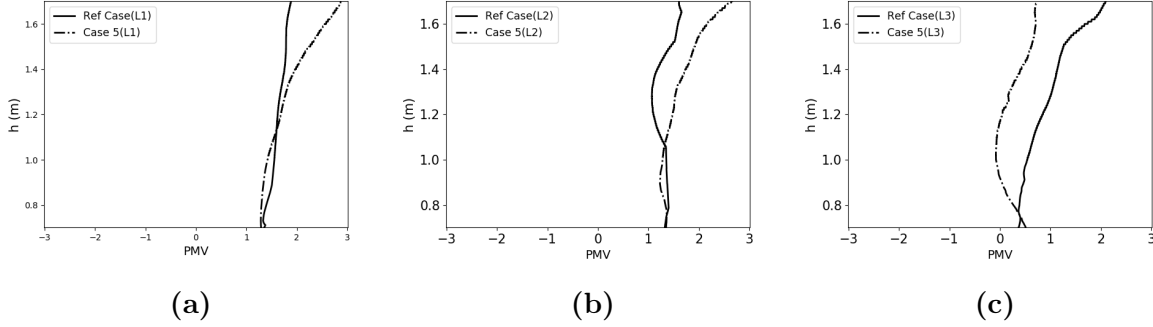


Figure 3.39: PMV profiles for case 5 and reference case along (a) line 1, (b) line 2, and (c) line 3 ($t = 200s$).

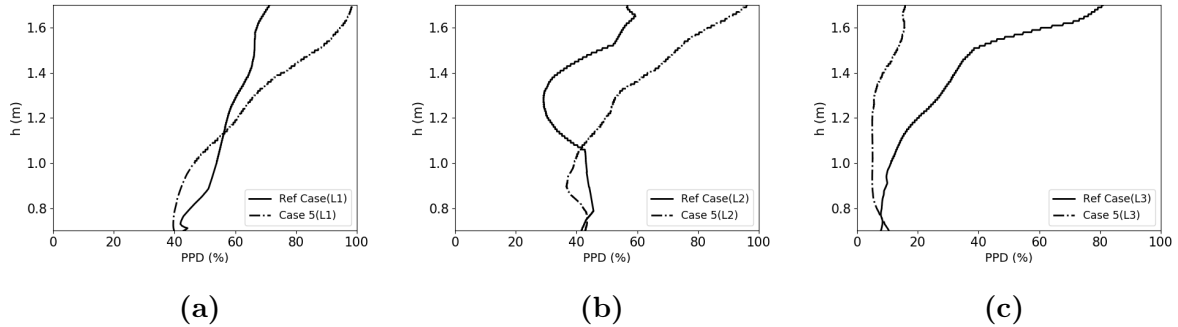


Figure 3.40: PPD profiles for case 5 and reference case along (a) line 1, (b) line 2, and (c) line 3 ($t = 200s$).

3.2.6 Impact of Number of Exhaust Vents

In this part, the effect of multiple outlet vents on the airflow is investigated. For this purpose, two output vents are located at the front and the back of the ceiling (vent 1 and vent 4), and the inlet is located at vent 2. Details about assigned vents as inlet and outlets are listed in Table 3.9. All vents have a same size of $0.36 \times 0.36 m^2$. Temperature and

Table 3.9: Vent coordinates for case 6 and the reference case.

Scenario	Inlet	Outlet 1	Outlet 2	Center of inlet			Center of outlet 1			Center of outlet 2		
	location	location	location	X(m)	Y(m)	Z(m)	X(m)	Y(m)	Z(m)	X(m)	Y(m)	Z(m)
Reference Case	vent 3	vent 1	---	3.78	2.027	0	1.57	2.027	0	---	---	---
Case 6	vent 2	vent 1	vent 4	3.78	2.027	0	1.57	2.027	0	4.38	2.027	0

velocity magnitude contours are depicted in Figure 3.41, 3.42, 3.43, and 3.44. Compare to the reference case, fresh airflows more efficiently and the recirculation zone at the top of the cabin become smaller compared to the reference case. In addition, for case 6 where the inlet is located in the middle of the ceiling, the entrainment and the impinging momentum distribute on all sides. This process leads to more effective cooling. Therefore, the new case (case 6) represents a lower temperature at the front and most of the middle areas. This claim is supported by temperature, PMV and PPD diagram at line 1 and line 2 in Figure 3.45, 3.46, and 3.47. Although temperature profiles for both cases almost overlap each other at line 3, the PMV and PPD diagrams show discrepancy at the rear parts of the cabin. Moreover, case 6 shows a uniform behavior for temperature, PMV, and PPD at line 3.

It is clear that selecting the right location for the outlet vents has a significant impact on the effectiveness of an AC system for an RV.

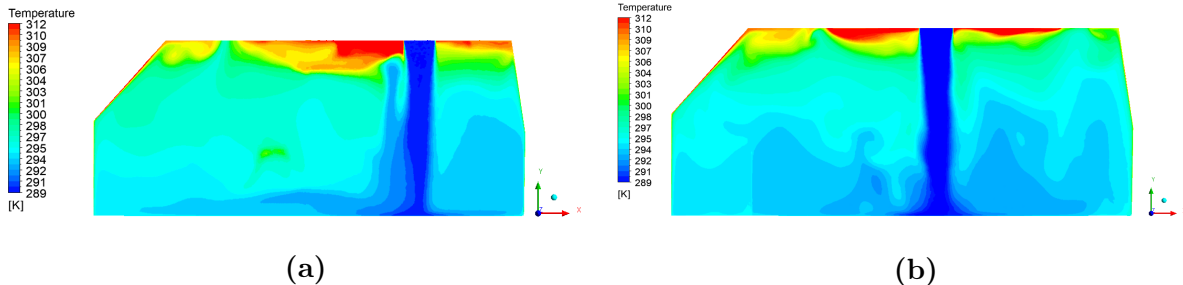


Figure 3.41: Temperature distribution at $Z = 0m$ for (a) reference case (b) case 6 ($t = 200s$).

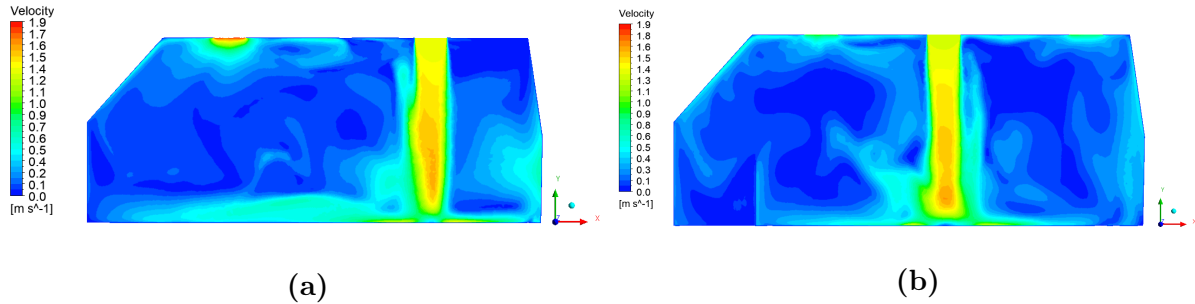


Figure 3.42: Velocity magnitude at $Z = 0m$ for (a) reference case (b) case 6 ($t = 200s$).

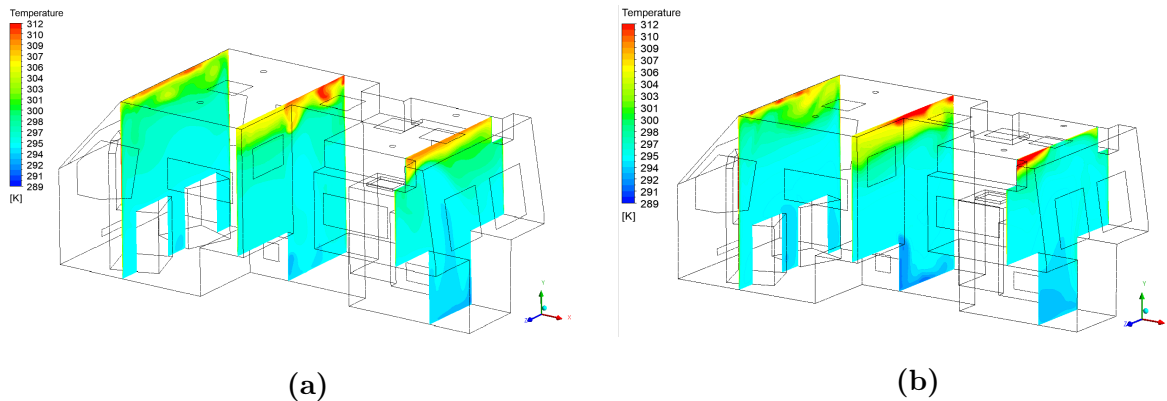


Figure 3.43: Temperature distribution at $X = 0.86m$, $X = 2.4m$, $X = 4.5m$ for (a) reference case (b) case 6 ($t = 200s$).

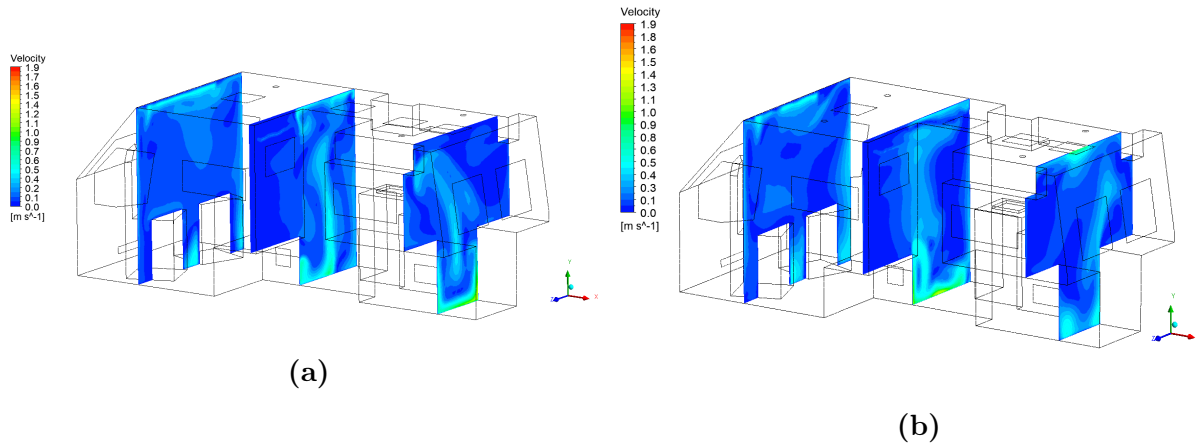


Figure 3.44: Velocity magnitude at $X = 0.86m$, $X = 2.4m$, $X = 4.5m$ for (a) reference case (b) case 6 ($t = 200s$).

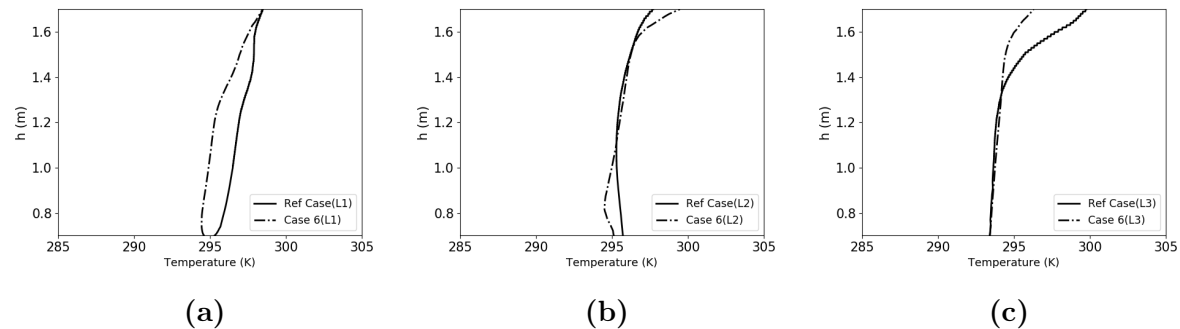


Figure 3.45: Temperature profiles for case 6, and reference case along (a) line 1, (b) line 2, and (c) line 3 ($t = 200s$).

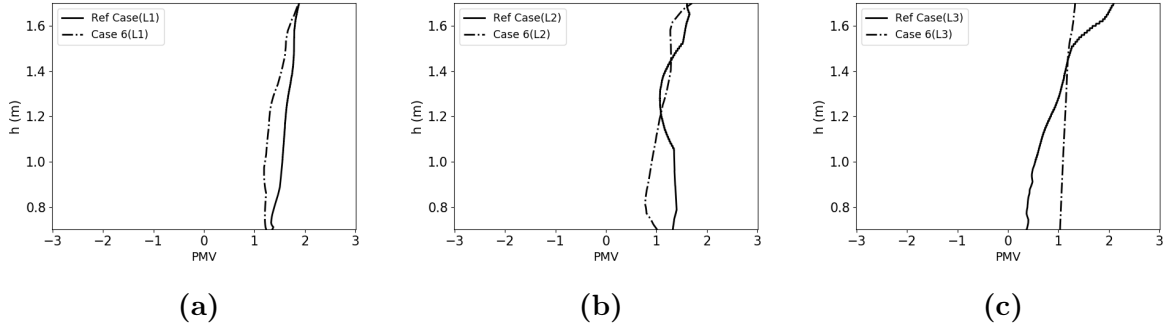


Figure 3.46: PMV profiles for case 6 and reference case along (a) line 1, (b) line 2, and (c) line 3 ($t = 200s$).

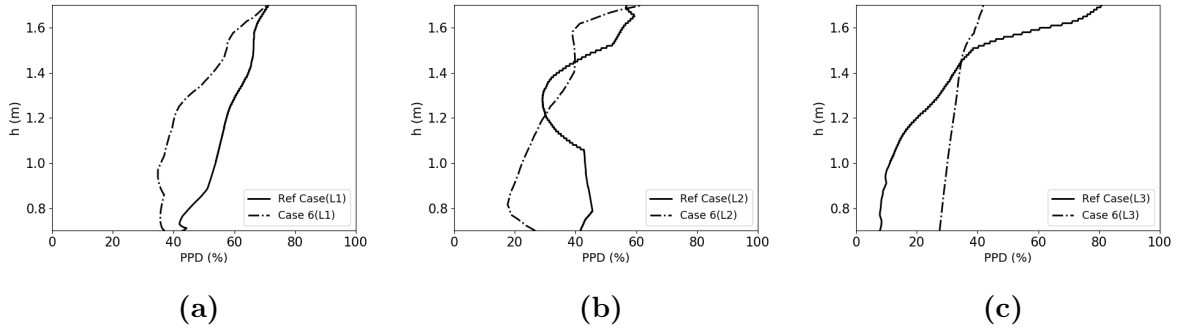


Figure 3.47: PPD profiles for case 6 and reference case along (a) line 1, (b) line 2, and (c) line 3 ($t = 200s$).

3.2.7 Summary of Results

A parametric study was done to investigate the air circulation and temperature distribution inside the RV's cabin for different conditions. A base model was created and used as a reference case, and further changes were applied to this case, in a parametric fashion, to determine their effects. The results from the previous sections showed the impact of

different parameters, including supply airflow direction, the AC inlet location, the exhaust vent location, and number of the output vents. The results mentioned in this section only applied to thermal comfort within the cabin.

Studying the angle at which the air enters the cabin through the inlet port showed that the reference case where the air entered the space vertically, provided more a desirable PMV profile along all three designated lines. In terms of the locations for inlet and outlet vents, the results showed that case 3 (with inlet vent at the geometric center along the ceiling) was more advantageous at line 1.

However, at line 2, all cases (reference case, case 3, and case 4) showed the same behavior. At line 3, the reference case was deemed the best. Investigation of the outlet vent location showed that case 5 (with outlet located at the back of the cabin) had the most desirable PMV at line 3. In addition, at line 1, PMV values for the reference case and case 5 overlaps. At line 2, reference case showed the best results.

Finally, by using an extra outlet in case 6 (two outlets at both sides of the inlet vent), a better distribution was observed at lines 1 and 2. At line 3, the reference case had a smaller PMV value; however, case 6 had a uniform behavior for PMV at this line.

Overall, the results of this parametric study showed that case 6 should be selected as the most optimized case with the most desirable PMV value. The spatial-averaged temperature versus time for case 6 and the reference case are compared in Figure 3.48. Clearly case 6 leads to a lower average temperature at all time because the cold air circulate more efficiently.

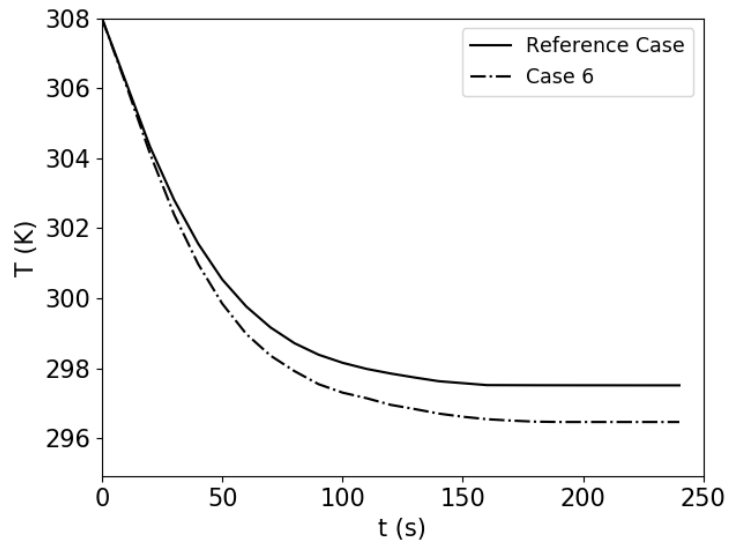


Figure 3.48: Transient simulation of spatial-averaged temperature for reference case and case 6 (two outlets at both sides of the inlet vent).

Chapter 4

Conclusions

Thermal comfort is becoming an integral part of most vehicles' design processes. Currently, no clear guidelines exist for determining thermal comfort within recreational vehicles, so designers have to rely on good practices, which are not sufficient for optimal designs. It is necessary to study thermal comfort within vehicles with more advanced techniques to draw better conclusions. This work focused on evaluating the thermal comfort within an RV using computational fluid dynamics. For this purpose, two main variables were studied, namely the temperature and air velocity within a given space. The approach for evaluating thermal comfort was based on ASHRAE 55 and the PMV methods.

It isn't very easy to assess thermal comfort in a realistic situation. There are analytical, numerical, and experimental methods for doing so. However, the analytical methods cannot account for the complexity of the geometry and flow in realistic flows, and the experimental methods are too costly. Therefore, a numerical approach towards calculating thermal comfort was selected and performed using CFD analyses. The downside in using CFD models is that it may generate inaccurate results, and hence, it has to be validated against

existing models or experimental results.

Firstly, to show the reliability of numerical solutions in simulating the airflow distribution in a domain, a room with a heat source and two open vents was numerically modeled with a 3D steady RANS CFD simulation. The results for temperature were compared with experimental data gathered by Li [2] and additional CFD results generated by [83] based on the same experimental data. In the referenced experiment, the temperatures were recorded along a single vertical pole at the steady-state condition. The CFD results were in good agreement with the experimental data from this experiment. This exercise showed the capability of the numerical approach in reproducing the thermal environment and the airflow pattern inside the test domain. As a result, the CFD model was deemed accurate for studying the impact of several design choices on thermal comfort within buildings and vehicle compartments.

The CFD model of a representative RV was described in detail in Chapter 3. This study was divided into two main parts. The first part presented a reference case that was based on the existing assumptions and limitations. For further optimizations with respect to this reference case, a parametric study is proposed in the second part. This parametric study focused on investigating the impact of AC inlet and outlet vent locations, supply airflow direction, and varying the number of exhaust vents. Seven test cases were simulated in total. The simulation results were evaluated through their temperatures, velocity magnitudes, PMV, and PPD values. The details regarding the optimizations are briefly presented in the following paragraphs.

The first studied parameter was the direction of the supply airflow. The results showed that the reference case resulted in better mixing of air as well as having lower PMV, PPD, and temperature values at the studied locations compared to the two other cases.

The second parameter was the locations for the inlet vents within the RV. It was shown that placing the inlet closer to the outlet port lead to inefficient mixing of the air. In this case, the temperature at the driver seat region was lower, and thereby, the PMV value was in the cold range in this location. On the other hand, for the cases in which the inlet and outlet were farther from each other, the air mixing was better, and PMV and PPD values were more uniforms along the studied lines.

Next, the impact of outlet vent location was investigated. The study showed case 5, where the outlet was next to the inlet at the back of the vehicle along with the ceiling, lead to better air circulation within the cabin, especially at the rear region close to the bed. For line 2 and line 1, both case 5 and reference case had approximately the same behavior regarding the PMV and PPD values.

The last parameter of interest was the number of exhaust vents. In this section, the results showed that increasing the number of outlet vents and selecting the right placement for the outlets substantially improved the air mixing within the RV. This study revealed that case 6 resulted in the highest degree of thermal comfort within the space relative to the reference case. This was determined to be due to the improved mixing of air that was induced by locating the inlet air vent at the center and two outlet vents at the sides of the vehicle.

As detailed in the preceding paragraphs, a handful of design parameters can have a considerable effect on the thermal comfort within the same vehicle. One of the main takeaways from this study was that the supply air should be sent into the cabin vertically to induce better mixing. The results revealed that adjusting the angle for the supply air does not provide any benefits to the thermal comfort metrics and should not be attempted for vehicles with this geometry. On the other hand, the results showed that having two exhaust vents improved the mixing within the cabin significantly and minimized the size

of hot spots. Hence, the designers should consider having multiple exhaust vents in the HVAC systems. Best practices for optimal designs in terms of thermal comfort cannot be generalized and could vary substantially from one vehicle to another. Complete optimization of HVAC systems is considered as a formidable task and is beyond the scope of the current study. Therefore, the designers must be aware of these effects and incorporate CFD analyses into the design development to make more informed design decisions.

4.1 Future Work

The work presented in this study had many limitations attached to it due to the time constraints. However, many of these assumptions and constraints can be better addressed through further studies.

Firstly, the time duration used for this study is too short for evaluating actual energy savings in RVs, because day-long simulations are required, which would correctly account for the thermostatic controls within the vehicle, and the thermal mass of the items within the cabins. To do so, the CFD model has to be coupled with a Vapour Compression Refrigeration (VCR) cycle in Matlab/Simulink or any compatible software to keep track of the energy consumed by the HVAC system for different cases. This would allow optimization of the HVAC systems both in terms of thermal comfort and energy consumption. Furthermore, the humidity ratio was considered constant; however, the impact of considering variable humidity ratio may be worth investigating. Lastly, the ambient conditions used in this model were treated as constants based on previous studies; however, the model can be used to assess the thermal comfort criteria for different locations where the vehicle may be operating. This would have a significant impact on the temperature distributions within the RV, and further investigations are required.

References

- [1] P.-A. Danca, “Ventilation strategies for improving the indoor environment quality in vehicles,” 2018.
- [2] Y. Li, M. Sandberg, and L. Fuchs, “Effects of thermal radiation on airflow with displacement ventilation: an experimental investigation,” *Energy and buildings*, vol. 19, no. 4, pp. 263–274, 1993.
- [3] “Specification Sheets, Personal communication with the Aktiv project manager,” 2018.
- [4] ASHRAE, “Thermal environmental conditions for human occupancy, ANSI/ASHRAE Standard 55-2013,” *American Society of Heating, Refrigerating and Air-Conditioning Engineers, Atlanta, GA*, 2013.
- [5] W. Frei, “Meshing Considerations for Linear Static Problems,” URL: <https://www.comsol.com/blogs/meshing-considerations-linear-static-problems/>, 2013.
- [6] L. Pérez-Lombard, J. Ortiz, and C. Pout, “A review on buildings energy consumption information,” *Energy and buildings*, vol. 40, no. 3, pp. 394–398, 2008.

- [7] K. J. Chua, S. K. Chou, W. M. Yang, and J. Yan, “Achieving better energy-efficient air conditioning—a review of technologies and strategies,” *Applied Energy*, vol. 104, pp. 87–104, 2013.
- [8] L. J. Schoen, P. F. Alspach, E. A. Arens, R. M. Aynsley, R. Bean, J. Eddy, D. Int-hout, E. E. Khalil, P. Simmonds, J. L. Stoops, S. C. Turner, W. F. Walter, R. L. Hall, J. R. Anderson, C. S. Barnaby, S. F. Bruning, J. A. Clark, S. J. Emmerich, and J. M. Ferguson, “Thermal Environmental Conditions for Human Occupancy,” vol. 2013, 2013.
- [9] J. L. M. Hensen, *On the thermal interaction of building structure and heating and ventilating system*. Technische Universiteit Eindhoven, 1991.
- [10] Z. Lin and S. Deng, “A study on the thermal comfort in sleeping environments in the subtropics—developing a thermal comfort model for sleeping environments,” *Building and Environment*, vol. 43, no. 1, pp. 70–81, 2008.
- [11] N. Djongyang, R. Tchinda, and D. Njomo, “Thermal comfort: A review paper,” *Renewable and sustainable energy reviews*, vol. 14, no. 9, pp. 2626–2640, 2010.
- [12] L. D. Frank, M. A. Andresen, and T. L. Schmid, “Obesity relationships with community design, physical activity, and time spent in cars,” *American journal of preventive medicine*, vol. 27, no. 2, pp. 87–96, 2004.
- [13] P. Taylor, R. J. Fuller, and M. B. Luther, “Energy use and thermal comfort in a rammed earth office building,” *Energy and buildings*, vol. 40, no. 5, pp. 793–800, 2008.
- [14] A. Wagner, E. Gossauer, C. Moosmann, T. Gropp, and R. Leonhart, “Thermal comfort and workplace occupant satisfaction—Results of field studies in German low energy office buildings,” *Energy and Buildings*, vol. 39, no. 7, pp. 758–769, 2007.

- [15] R. Farrington, M. Cuddy, M. Keyser, and J. Rugh, “Opportunities to reduce air-conditioning loads through lower cabin soak temperatures,” tech. rep., 1999.
- [16] J. P. Rugh, R. B. Farrington, D. Bharathan, A. Vlahinos, R. Burke, C. Huizenga, and H. Zhang, “Predicting human thermal comfort in a transient nonuniform thermal environment,” *European journal of applied physiology*, vol. 92, no. 6, pp. 721–727, 2004.
- [17] R. B. Farrington, R. Anderson, D. M. Blake, S. D. Burch, M. R. Cuddy, M. A. Keyser, and J. P. Rugh, “Challenges and potential solutions for reducing climate control loads in conventional and hybrid electric vehicles,” *National Renewable Energy Laboratory, Golden, CO, USA, Download from: www.ott.doe.gov/coolcar/pubs.html*, 1999.
- [18] Internaional Energy Agency, “Report on CO₂ emissions from fuel combustion,” tech. rep., International Energy Agency, 2013.
- [19] R. Haass, P. Dittmer, M. Veigt, and M. Lütjen, “Reducing food losses and carbon emission by using autonomous control—A simulation study of the intelligent container,” *International Journal of Production Economics*, vol. 164, pp. 400–408, 2015.
- [20] M. A. Fayazbakhsh, *Energy-Smart Calculation of Thermal Loads in Mobile and Stationary Heating, Ventilation, Air Conditioning, and Refrigeration Systems*. PhD thesis, 2015.
- [21] M. A. Lambert and B. J. Jones, “Automotive adsorption air conditioner powered by exhaust heat. Part 1: conceptual and embodiment design,” *Proceedings of the Institution of Mechanical Engineers, Part D: Journal of Automobile Engineering*, vol. 220, no. 7, pp. 959–972, 2006.

- [22] J. S. Welstand, H. H. Haskew, R. F. Gunst, and O. M. Bevilacqua, “Evaluation of the effects of air conditioning operation and associated environmental conditions on vehicle emissions and fuel economy,” *SAE transactions*, pp. 1993–2006, 2003.
- [23] P. Fanger, “Thermal Comfort-Analysis and Applications in Environmental Engineering,” *in: C.D.T. Press. (Ed.)*, 1970.
- [24] A. Vartires, A. Dogeanu, and P. Dancă, “The human thermal comfort evaluation inside the passenger compartment, Air pollution and climate change,” *Energy and Clean Technologies Conference Proceedings*, p. 8, 2015.
- [25] W. Zhang, J. Chen, and F. Lan, “Experimental study on occupant’s thermal responses under the non-uniform conditions in vehicle cabin during the heating period,” *Chinese Journal of Mechanical Engineering*, 2014.
- [26] ISO, “Ergonomics of the thermal environment, Evaluation of thermal environments in vehicles Part 1: Principles and methods for assessment of thermal stress, in: ISO 14505-1:2007,” 2007.
- [27] ISO, “Ergonomics of the thermal environment - Evaluation of thermal environments in vehicles - Part 2: Determination of equivalent temperature in: ISO 14505-2:2006,” 2006.
- [28] ISO, “Ergonomics of the thermal environment -Evaluation of thermal environments in vehicles Part 3: Evaluation of thermal comfort using human subjects, in: ISO 14505-3:2006,” 2006.
- [29] P. Danca, A. Vartires, and A. Dogeanu, “An overview of current methods for thermal comfort assessment in vehicle cabin,” *Energy Procedia*, vol. 85, pp. 162–169, 2016.

- [30] P. Danca, F. Bode, I. Nastase, and A. Meslem, “On the Possibility of CFD Modeling of the Indoor Environment in a Vehicle.,” *Energy Procedia* 112, pp. 656–663, 2017.
- [31] H. Oi, K. Tabata, Y. Naka, A. Takeda, and Y. Tochihara, “Effects of heated seats in vehicles on thermal comfort during the initial warm-up period,” *Applied Ergonomics*, vol. 43, no. 2, pp. 360–367, 2012.
- [32] T. G. Cengiz and F. C. Babalık, “An on-the-road experiment into the thermal comfort of car seats,” *Applied Ergonomics*, vol. 38, no. 3, pp. 337–347, 2007.
- [33] A. Alahmer, M. Abdelhamid, and M. Omar, “Design for thermal sensation and comfort states in vehicles cabins,” *Applied Thermal Engineering*, vol. 36, pp. 126–140, 2012.
- [34] O. Kaynakli and M. Kilic, “An investigation of thermal comfort inside an automobile during the heating period,” *Applied ergonomics*, vol. 36, no. 3, pp. 301–312, 2005.
- [35] O. Kaynakli, U. Unver, and M. Kilic, “Evaluating thermal environments for sitting and standing posture,” *International Communications in Heat and Mass Transfer*, vol. 30, no. 8, pp. 1179–1188, 2003.
- [36] F. Kalmár and T. Kalmár, “Interrelation between mean radiant temperature and room geometry,” *Energy and Buildings*, vol. 55, pp. 414–421, 2012.
- [37] W. Liu, Z. Lian, Q. Deng, and Y. Liu, “Evaluation of calculation methods of mean skin temperature for use in thermal comfort study,” *Building and Environment*, vol. 46, no. 2, pp. 478–488, 2011.
- [38] E. Barna and L. Bánhidi, “Combined effect of two local discomfort parameters studied with a thermal manikin and human subjects,” *Energy and Buildings*, vol. 51, pp. 234–241, 2012.

- [39] F. R. d. Alfano, M. Dell’Isola, B. I. Palella, G. Riccio, and A. Russi, “On the measurement of the mean radiant temperature and its influence on the indoor thermal environment assessment,” *Building and Environment*, vol. 63, pp. 79–88, 2013.
- [40] N. Arslanoglu and A. Yigit, “Experimental and theoretical investigation of the effect of radiation heat flux on human thermal comfort,” *Energy and Buildings*, vol. 113, pp. 23–29, 2016.
- [41] R. Z. Homod, “Review on the HVAC System Modeling Types and the Shortcomings of Their Application,” *Journal of Energy*, vol. 2013, pp. 1–10, 2013.
- [42] Q. Zhang and M. Canova, “Lumped-Parameter Modeling of an Automotive Air Conditioning System for Energy Optimization and Management,” in *ASME Dynamic Systems and Control Conference*, pp. 1–8, 2013.
- [43] V. S. Harish and A. Kumar, “A review on modeling and simulation of building energy systems,” *Renewable and Sustainable Energy Reviews*, vol. 56, pp. 1272–1292, 2016.
- [44] M. M. Gouda, S. Danaher, and C. P. Underwood, “Building thermal model reduction using nonlinear constrained optimization,” *Building and Environment*, vol. 37, no. 12, pp. 1255–1265, 2002.
- [45] E. Samadiani, “Energy efficient thermal management of data centers via open multi-scale design,” no. December, 2009.
- [46] E. Samadiani and Y. Joshi, “Reduced order thermal modeling of data centers via proper orthogonal decomposition: a review,” *International Journal of Numerical Methods for Heat & Fluid Flow*, vol. 20, no. 5, pp. 529–550, 2010.

- [47] P. Weissler, “Federal lab cost-effectively eliminates diesel idling to condition Class 8 sleeper cabs,” *Automotive Engineering*, 2016.
- [48] T. Kiss, J. Lustbader, and D. Leighton, “Modeling of an Electric Vehicle Thermal Management System in MATLAB / Simulink,” *SAE Technical Paper*, no. April, pp. 21–23, 2015.
- [49] Q. Zhang, S. Eben Li, and K. Deng, *Automotive Air Conditioning: Optimization, Control and Diagnosis*. No. 2016, springer ed., 2002.
- [50] D. Sørensen and L. Voigt, “Modelling flow and heat transfer around a seated human body by computational fluid dynamics,” *Building and environment*, vol. 38, no. 6, pp. 753–762, 2003.
- [51] M. Salmanzadeh, G. Zahedi, G. Ahmadi, D. R. Marr, and M. Glauser, “Computational modeling of effects of thermal plume adjacent to the body on the indoor airflow and particle transport,” *Journal of Aerosol Science*, vol. 53, pp. 29–39, 2012.
- [52] W. A. Abdelmaksoud and E. E. Khalil, “Energy savings and thermal comfort optimization in office cubicle environment,” *ASHRAE Transactions*, vol. 121, no. 1, pp. 232–241, 2015.
- [53] O. Yongson, I. A. Badruddin, Z. A. Zainal, and P. A. Narayana, “Airflow analysis in an air conditioning room,” *Building and environment*, vol. 42, no. 3, pp. 1531–1537, 2007.
- [54] A. Fujita, J.-i. Kanemaru, H. Nakagawa, and Y. Ozeki, “Numerical simulation method to predict the thermal environment inside a car cabin,” *JSAE review*, vol. 22, no. 1, pp. 39–47, 2001.

- [55] A. Alexandrov, V. Kudriavtsev, and M. Reggio, “Analysis of flow patterns and heat transfer in generic passenger car mini-environment,” in *9th Annual Conference of the CFD Society of Canada*, pp. 27–29, Citeseer, 2001.
- [56] H. Zhang, L. Dai, G. Xu, Y. Li, W. Chen, and W.-Q. Tao, “Studies of air-flow and temperature fields inside a passenger compartment for improving thermal comfort and saving energy. Part I: Test/numerical model and validation,” *Applied Thermal Engineering*, vol. 29, no. 10, pp. 2022–2027, 2009.
- [57] H. Zhang, L. Dai, G. Xu, Y. Li, W. Chen, and W. Tao, “Studies of air-flow and temperature fields inside a passenger compartment for improving thermal comfort and saving energy. Part II: Simulation results and discussion,” *Applied Thermal Engineering*, vol. 29, no. 10, pp. 2028–2036, 2009.
- [58] J. Jonsson, “Including solar load in CFD analysis of temperature distribution in a car passenger compartment,” 2007.
- [59] T. Han and K.-H. Chen, “Assessment of various environmental thermal loads on passenger compartment soak and cool-down analyses,” tech. rep., 2009.
- [60] T. Ye, “A Statistical Approach for Correlation/Validation of Hot-Soak Terminal Temperature of a Vehicle Cabin CFD Model,” *SAE Technical Paper Series*, vol. 1, 2013.
- [61] H. K. Versteeg and W. Malalasekera, *An Introduction to Computational Fluid Dynamics The Finite Volume Method*. second edi ed., 2007.
- [62] Q. Chen, Z. Zhang, and W. Zuo, “Computational fluid dynamics for indoor environment modeling: past, present and future,” in *Proceedings XXV Congresso della Trasmissione del Calore UIT, Trieste*, 2007.

- [63] Z. Zhang, W. Zhang, Z. J. Zhai, and Q. Y. Chen, “Evaluation of various turbulence models in predicting airflow and turbulence in enclosed environments by CFD: Part 2—Comparison with experimental data from literature,” *Hvac&R Research*, vol. 13, no. 6, pp. 871–886, 2007.
- [64] S. R. S. A. O. V. Y. G. Karniadakis, A. Yakhot, “Proc. Seventh Symp. on Turbulent Shear Flows,” in *Proc. Seventh Symp. on Turbulent Shear Flows*, (Standford, CA), Standford University Press, 1989.
- [65] Z. Han and R. D. Reitz, “Turbulence modeling of internal combustion engines using RNG κ - ϵ models,” *Combustion science and technology*, vol. 106, no. 4-6, pp. 267–295, 1995.
- [66] V. Yakhot, S. A. Orszag, S. Thangam, T. B. Gatski, and C. G. Speziale, “Development of turbulence models for shear flows by a double expansion technique,” *Physics of Fluids A: Fluid Dynamics*, vol. 4, no. 7, pp. 1510–1520, 1992.
- [67] A. Meslem, A. Dia, C. Beghein, M. El Hassan, I. Nastase, and P.-J. Vialle, “A comparison of three turbulence models for the prediction of parallel lobed jets in perforated panel optimization,” *Building and Environment*, vol. 46, no. 11, pp. 2203–2219, 2011.
- [68] Q. Chen, “Ventilation performance prediction for buildings: A method overview and recent applications,” *Building and environment*, vol. 44, no. 4, pp. 848–858, 2009.
- [69] B. Blocken, “50 years of computational wind engineering: past, present and future,” *Journal of Wind Engineering and Industrial Aerodynamics*, vol. 129, pp. 69–102, 2014.
- [70] Y. Tominaga, A. Mochida, R. Yoshie, H. Kataoka, T. Nozu, M. Yoshikawa, and T. Shirasawa, “AIJ guidelines for practical applications of CFD to pedestrian wind environ-

ment around buildings,” *Journal of wind engineering and industrial aerodynamics*, vol. 96, no. 10-11, pp. 1749–1761, 2008.

- [71] M. Cook, P. Cropper, D. Fiala, R. Yousaf, S. Bolineni, and C. van Treeck, “Coupled CFD and Thermal Comfort Modeling in Cross-Ventilated Classrooms.,” *ASHRAE Transactions*, vol. 119, no. 2, 2013.
- [72] N. Kobayashi and Q. Chen, “Floor-supply displacement ventilation in a small office,” *Indoor and Built Environment*, vol. 12, no. 4, pp. 281–291, 2003.
- [73] M. J. Cook and K. J. Lomas, “Buoyancy-driven displacement ventilation flows: evaluation of two eddy viscosity turbulence models for prediction,” *Building Services Engineering Research and Technology*, vol. 19, no. 1, pp. 15–21, 1998.
- [74] Y. Ji, M. J. Cook, and V. Hanby, “CFD modelling of natural displacement ventilation in an enclosure connected to an atrium,” *Building and Environment*, vol. 42, no. 3, pp. 1158–1172, 2007.
- [75] P.-C. Liu, H.-T. Lin, and J.-H. Chou, “Evaluation of buoyancy-driven ventilation in atrium buildings using computational fluid dynamics and reduced-scale air model,” *Building and Environment*, vol. 44, no. 9, pp. 1970–1979, 2009.
- [76] C. Walker, G. Tan, and L. Glicksman, “Reduced-scale building model and numerical investigations to buoyancy-driven natural ventilation,” *Energy and Buildings*, vol. 43, no. 9, pp. 2404–2413, 2011.
- [77] Z. Lin, T. T. Chow, Q. Wang, K. F. Fong, and L. S. Chan, “Validation of CFD model for research into displacement ventilation,” *Architectural Science Review*, vol. 48, no. 4, pp. 305–316, 2005.

- [78] A. Stamou and I. Katsiris, “Verification of a CFD model for indoor airflow and heat transfer,” *Building and Environment*, vol. 41, no. 9, pp. 1171–1181, 2006.
- [79] T. Zhang, K. Lee, and Q. Chen, “A simplified approach to describe complex diffusers in displacement ventilation for CFD simulations,” *Indoor Air*, vol. 19, no. 3, pp. 255–267, 2009.
- [80] Z. J. Zhai, Z. Zhang, W. Zhang, and Q. Y. Chen, “Evaluation of various turbulence models in predicting airflow and turbulence in enclosed environments by CFD: Part 1—Summary of prevalent turbulence models,” *Hvac&R Research*, vol. 13, no. 6, pp. 853–870, 2007.
- [81] S. Hussain, P. H. Oosthuizen, and A. Kalendar, “Evaluation of various turbulence models for the prediction of the airflow and temperature distributions in atria,” *Energy and Buildings*, vol. 48, pp. 18–28, 2012.
- [82] Y. Li, M. Sandberg, and L. Fuchs, “Vertical temperature profiles in rooms ventilated by displacement: full-scale measurement and nodal modelling,” *Indoor Air*, vol. 2, no. 4, pp. 225–243, 1992.
- [83] S. Gilani, H. Montazeri, and B. Blocken, “CFD simulation of stratified indoor environment in displacement ventilation: Validation and sensitivity analysis,” *Building and Environment*, vol. 95, pp. 299–313, 2016.
- [84] K. Lee, “2017 Hymer Aktiv Review,” URL: <https://www.rvguide.com/manufacturer-other/2017-hymer-aktiv-review-1691.html>, 2017.
- [85] “2018 Hymer Aktiv,” URL: https://www.outdoorsy.com/rv-rental/pleasant-hill_ca/2018_hymer_aktiv_48629-listing, 2018.

- [86] H. Park, M. Ruellan, N. Martaj, R. Bennacer, and E. Monmasson, “Generic thermal model of electric appliances integrated in low energy building,” in *IECON 2012-38th Annual Conference on IEEE Industrial Electronics Society*, pp. 3318–3323, IEEE, 2012.
- [87] J. E. Jaramillo, C.-D. Perez-Segarra, I. Rodriguez, and A. Oliva, “Numerical study of plane and round impinging jets using RANS models,” *Numerical Heat Transfer, Part B: Fundamentals*, vol. 54, no. 3, pp. 213–237, 2008.
- [88] L. Huang and T. Han, “Validation of 3-D passenger compartment hot soak and cool-down analysis for virtual thermal comfort engineering,” tech. rep., 2002.
- [89] N. Ningbai, “Analysis of air flow distribution and thermal comfort in a hybrid electric vehicle,” 2014.

Appendices

Python code for calculating PMV and PPD values

```
# PMV analysis
# Written by Mahboube Taftian
import numpy as np
from math import exp, sqrt
import matplotlib.pyplot as plt
#CLO;      Clothing (clo)
#RH;       Relative humidity (%)
#PA;       Water vapour pressure (Pa)
#TA;       Air temperature (C)
#W;        External work, W/m2
#VEL;      Relative air velocity (m/s)
#MW;       Internal heat production in the human body, W/m2
#MET;      Metabolic rate (met)
#TR;       Mean radiant temperature (C)
#FNPS;     Saturated vapour pressure, kPa
#WME;      External work, normally around 0 (met)
```

$\#M;$	<i>Metabolic rate , W/m²</i>
$\#TCL;$	<i>Clothing surface temperature (C)</i>
$\#HCF;$	<i>Forced convective heat transfer coefficient , W/m²K</i>
$\#ICL;$	<i>Clothing insulation , m²K/W</i>
$\#TAA;$	<i>Air temperature , K</i>
$\#FCL;$	<i>Clothing area factor</i>
$\#HC;$	<i>Convective heat transfer coefficient , W/m²K</i>
$\#TS;$	<i>Thermal sensation transfer coefficient</i>
$\#TRA;$	<i>Mean radiant temperature , K</i>
$\#TCLA;$	<i>First guess for surface temperature of clothing</i>
$\#HCN;$	<i>Natural convective heat transfer coefficient , W/m²K</i>
$\#i;$	<i>Iterator</i>
$\#EPS;$	<i>Small value</i>
$\#P5;$	<i>Calculation terms</i>
$\#P3, P4;$	<i>Calculation terms</i>
$\#P1, P2;$	<i>Calculation terms</i>
$\#PPD;$	<i>predicted percentage dissatisfied</i>
$\#PMV;$	<i>Predicted mean vote</i>
$\#XN;$	<i>Iterative solutions</i>
$\#XF;$	<i>Iterative solutions</i>
$\#HL6;$	<i>Heat loss by convection</i>
$\#HL5;$	<i>Heat loss by radiation</i>
$\#HL4;$	<i>Dry respiration heat loss</i>
$\#HL3;$	<i>Latent respiration heat loss</i>
$\#HL2;$	<i>Heat loss by sweating (comfort)</i>

```

#HL1;      Heat loss difference through skin

FileNumber = 10
LineNumber = 3
PointNumber = 1000

Hight = np.zeros((FileNumber , LineNumber , PointNumber))
Temperature = np.zeros((FileNumber , LineNumber , PointNumber))
Vel_X = np.zeros((FileNumber , LineNumber , PointNumber))
Vel_Y = np.zeros((FileNumber , LineNumber , PointNumber))
Vel_Z = np.zeros((FileNumber , LineNumber , PointNumber))

for F in range(FileNumber):
    Filename = 'f' + '%0i'%F + ',temp.txt'
    with open (Filename , 'r') as fin:
        for L in range(LineNumber):
            line = fin.readline()
            for P in range(PointNumber):
                line = fin.readline()
                Temperature[F,L,P] = float(line.split()[0])
                Hight [F,L,P] = float(line.split()[1])

```

```

for F in range(FileNumber):
    Filename = 'f' + '%0i'%F + ',u.txt'
    with open (Filename , 'r') as fin:
        for L in range(LineNumber):
            line = fin . readline()
            for P in range(PointNumber):
                line = fin . readline()
                Vel_X[F,L,P] = float (line . split ()[0])
                Hight [F,L,P] = float (line . split ()[1])

for F in range(FileNumber):
    Filename = 'f' + '%0i'%F + ',v.txt'
    with open (Filename , 'r') as fin:
        for L in range(LineNumber):
            line = fin . readline()
            for P in range(PointNumber):

```

```

        line = fin.readline()
        Vel_Y[F,L,P] = float(line.split()[0])
        Hight[F,L,P] = float(line.split()[1])

for F in range(FileNumber):
    Filename = 'f' + '%0i'%F + ',w.txt'
    with open (Filename , 'r') as fin:
        for L in range(LineNumber):
            line = fin.readline()
            for P in range(PointNumber):
                line = fin.readline()
                Vel_Z[F,L,P] = float(line.split()[0])
                Hight[F,L,P] = float(line.split()[1])

PMV = np.zeros((FileNumber, LineNumber, PointNumber))
PPD = np.zeros((FileNumber, LineNumber, PointNumber))

for F in range(FileNumber):
    for L in range(LineNumber):
        for P in range(PointNumber):

```

TA = Temperature [F,L,P] - 273

UA = Vel_X[F,L,P]

VA = Vel_Y[F,L,P]

WA = Vel_Z[F,L,P]

EPS=0.00015

CLO=1.0

MET=1.0

WME=0.0

RH=50.0

ICL=0.155*CLO

M=MET*58.15

W=WME*58.15

MW=MW

if (ICL<=0.078):

FCL=1.0+1.29*ICL

else:

FCL=1.05+0.645*ICL

TR=35

VEL=sqrt(UA*UA + VA*VA + WA*WA)

FNPS=exp(16.6536 - 4030.183/(TA+235))

PA=RH*10.0*FNPS

HCF=12.1*sqrt(VEL)

TAA=TA+273.0

```

TRA=TR+273.0
TCLA=TAA+(35.5-TA) / ( 3.5*(6.45*ICL+0.1))
P1=ICL*FCL
P2=P1*3.96
P3=P1*100
P4=P1*TAA
P5=308.7-0.028*MW+P2*((TRA/100)**4)
XN=TCLA/100.0
XF=XN

for i in range(150):
    XF=(XF+XN)/2.0
    HCN=2.38*(abs(100.0*XF-TAA)**0.25)
    if (HCF>HCN):
        HC=HCF
    else:
        HC=HCN
    XN=(P5+P4*HC-P2*(XF**4))/(100+P3*HC)
    if (abs(XN-XF)<EPS):
        break

TCL=100.0*XN-273.0
HL1=3.05*0.001*(5733.0-6.99*MW*PA)
if (MW>58.15):
    HL2=0.42*(MW-58.15)

```

```

else :
    HL2 = 0
    HL3=1.7*0.00001*M*(5867.0-PA)
    HL4=0.0014*M*(34.0-TA)
    HL5=3.96*FCL*((XN**4)-((TRA/100.0)**4))
    HL6=FCL*HC*(TCL-TA)
    TS=0.303*exp(-0.036*M)+0.028
    PMV[F,L,P] = TS*(MW-HL1-HL2-HL3-HL4-HL5-HL6)
    PPD[F,L,P] = 100.0-95.0*exp(-0.03353*(PMV[F,L,P]**4)
        -0.2179*(PMV[F,L,P]**2))

plt.figure('Line1-PMV')
plt.plot(PMV[0,0,:], Hight[0,0,:], lw=2, c='k', linestyle='--',
label='Ref_Case(L1)')
plt.plot(PMV[6,0,:], Hight[6,0,:], lw=2, c='k', linestyle='-.',
label='Case_1(L1)')
plt.plot(PMV[7,0,:], Hight[7,0,:], lw=2, c='k', linestyle=':',
label='Case_2(L1)')
axes = plt.gca()
plt.rcParams.update({'font.size': 15})
axes.set_xlim([-3.01,3.01])
axes.set_ylim([0.7,1.7])
plt.xlabel('PMV', fontsize=14)
plt.ylabel('h(m)', fontsize=15)
plt.legend(loc='center_left', fontsize = 'small')

```

```

plt.figure('Line2-PMV')
plt.plot(PMV[0,1,:], Hight[0,1,:], lw=2, c='k', linestyle='-', label='Ref_Case(L2)')
plt.plot(PMV[6,1,:], Hight[6,1,:], lw=2, c='k', linestyle='-.', label='Case_1(L1)')
plt.plot(PMV[7,1,:], Hight[7,1,:], lw=2, c='k', linestyle=':', label='Case_2(L1)')
axes = plt.gca()
plt.rcParams.update({'font.size': 15})
axes.set_xlim([-3.01,3.01])
axes.set_ylim([0.7,1.7])
plt.xlabel('PMV', fontsize=14)
plt.ylabel('h(m)', fontsize=15)
plt.legend(loc='center_left', fontsize = 'small')

plt.figure('Line3-PMV')
plt.plot(PMV[0,2,:], Hight[0,2,:], lw=2, c='k', linestyle='-', label='Ref_Case(L3)')
plt.plot(PMV[6,2,:], Hight[6,2,:], lw=2, c='k', linestyle='-.', label='Case_1(L1)')
plt.plot(PMV[7,2,:], Hight[7,2,:], lw=2, c='k', linestyle=':', label='Case_2(L1)')
axes = plt.gca()
plt.rcParams.update({'font.size': 15})

```

```

axes.set_xlim([-3.01,3.01])
axes.set_ylim([0.7,1.7])
plt.xlabel('PMV', fontsize=14)
plt.ylabel('h(m)', fontsize=15)
plt.legend(loc='center_left', fontsize = 'small')

plt.figure('Line1-Temp')
plt.plot(Temperature[0,0,:], Hight[0,0,:], lw=2, c='k', linestyle='--',
label='Ref_Case(L1)')
plt.plot(Temperature[6,0,:], Hight[6,0,:], lw=2, c='k', linestyle='-.',
label='Case_1(L1)')
plt.plot(Temperature[7,0,:], Hight[7,0,:], lw=2, c='k', linestyle=': ',
label='Case_2(L1)')
axes = plt.gca()
plt.rcParams.update({'font.size': 15})
axes.set_xlim([289,312])
axes.set_ylim([0.7,1.7])
plt.xlabel('Temperature(K)', fontsize=13)
plt.ylabel('h(m)', fontsize=15)
plt.legend(loc='lower_right', fontsize = 'small')

plt.figure('Line2-Temp')
plt.plot(Temperature[0,1,:], Hight[0,1,:], lw=2, c='k', linestyle='--',
label='Ref_Case(L2)')
plt.plot(Temperature[6,1,:], Hight[6,1,:], lw=2, c='k', linestyle='-.',
label='Case_1(L2)')

```

```

label='Case_1(L1)')

plt.plot(Temperature[7,1,:], Hight[7,1,:], lw=2, c='k', linestyle=':',
label='Case_2(L1)')

axes = plt.gca()

plt.rcParams.update({'font.size': 15})

axes.set_xlim([289,312])
axes.set_ylim([0.7,1.7])

plt.xlabel('Temperature(K)', fontsize=13)
plt.ylabel('h(m)', fontsize=15)
plt.legend(loc='lower_right', fontsize = 'small')

plt.figure('Line3-Temp')

plt.plot(Temperature[0,2,:], Hight[0,2,:], lw=2, c='k', linestyle='--',
label='Ref_Case(L3)')

plt.plot(Temperature[6,2,:], Hight[6,2,:], lw=2, c='k', linestyle='-.',
label='Case_1(L1)')

plt.plot(Temperature[7,2,:], Hight[7,2,:], lw=2, c='k',
linestyle=':', label='Case_2(L1)')

axes = plt.gca()

plt.rcParams.update({'font.size': 15})

axes.set_xlim([289,312])
axes.set_ylim([0.7,1.7])

plt.xlabel('Temperature(K)', fontsize=13)
plt.ylabel('h(m)', fontsize=15)
plt.legend(loc='lower_right', fontsize = 'small')

```

```

plt.figure('Line1-PPD')
plt.plot(PPD[0,0,:], Hight[0,0,:], lw=2, c='k', linestyle='-', label='Ref_Case(L1)')
plt.plot(PPD[6,0,:], Hight[6,0,:], lw=2, c='k', linestyle='-.', label='Case_1(L1)')
plt.plot(PPD[7,0,:], Hight[7,0,:], lw=2, c='k', linestyle=':', label='Case_2(L1)')
axes = plt.gca()
plt.rcParams.update({'font.size': 15})
axes.set_xlim([0,100])
axes.set_ylim([0.7,1.7])
plt.xlabel('PPD(%)', fontsize=14)
plt.ylabel('h(m)', fontsize=15)
plt.legend(loc='lower_left', fontsize = 'small')

plt.figure('Line2-PPD')
plt.plot(PPD[0,1,:], Hight[0,1,:], lw=2, c='k', linestyle='-', label='Ref_Case(L2)')
plt.plot(PPD[6,1,:], Hight[6,1,:], lw=2, c='k', linestyle='-.', label='Case_1(L1)')
plt.plot(PPD[7,1,:], Hight[7,1,:], lw=2, c='k', linestyle=':', label='Case_2(L1)')
axes = plt.gca()
plt.rcParams.update({'font.size': 15})

```

```

axes.set_xlim([0,100])
axes.set_ylim([0.7,1.7])
plt.xlabel('PPD(%)', fontsize=14)
plt.ylabel('h(m)', fontsize=15)
plt.legend(loc='lower_left', fontsize = 'small')

plt.figure('Line3-PPD')
plt.plot(PPD[0,2,:], Hight[0,2,:], lw=2, c='k', linestyle='--',
label='Ref_Case(L3)')
plt.plot(PPD[6,2,:], Hight[6,2,:], lw=2, c='k', linestyle='-.',
label='Case_1(L1)')
plt.plot(PPD[7,2,:], Hight[7,2,:], lw=2, c='k', linestyle=':',
label='Case_2(L1)')
axes = plt.gca()
plt.rcParams.update({'font.size': 15})
axes.set_xlim([0,100])
axes.set_ylim([0.7,1.7])
plt.xlabel('PPD(%)', fontsize=14)
plt.ylabel('h(m)', fontsize=15)
plt.legend(loc='lower_left', fontsize = 'small')

```